Engineering Fracture Mechanics 289 (2023) 109471

Contents lists available at ScienceDirect

Engineering Fracture Mechanics

journal homepage: www.elsevier.com/locate/engfracmech

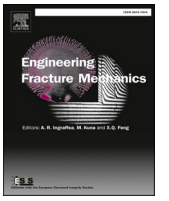

Anisotropic plasticity and fracture modelling of cold rolled AA5754

Borja Erice [a,b,*], Bernard Rolfe [c], Joseba Mendiguren [a]

[a] Mondragon Unibertsitatea, Faculty of Engineering, Department of Mechanics and Industrial Production, Loramendi 4, Arrasate-Mondragon 20500, Gipuzkoa, Spain
[b] IKERBASQUE, Basque Foundation for Science, Bilbao, Spain
[c] School of Engineering, Deakin University, Geelong, Australia

ARTICLE INFO

Keywords:
Anisotropy
Ductile fracture
Plasticity
Fracture initiation criterion
Aluminium

ABSTRACT

The effect of the anisotropy, the loading rate and stress state on the ductile fracture of AA5754 cold-rolled sheets has been investigated. The plasticity has been analysed experimentally testing biaxial and uniaxial tensile specimens machined at several orientations with respect to the rolling direction and calibrating the Yld2000-3D yield criterion. The strain rate dependency of the material has been evaluated testing notched tension specimens at different loading rates. The resulting force–displacement curves, showing negative loading rate sensitivity, have been employed to identify the work hardening constants of a modified isotropic rate-dependent law through inverse modelling. Finite element simulations of the experiments on central hole, notched, shear and biaxial specimens conducted at several loading rates and orientations, monitored with three-dimensional digital image correlation, have been performed to obtain the Cauchy stress and equivalent plastic strain histories from the critical elements located where fracture is observed in such experiments. The anisotropic Hosford-Coulomb fracture initiation criterion has been modified to accommodate the loading rate effects giving reasonable failure predictions.

1. Introduction

The sheet metal stamping is one of the most common and recurrent processes that allows obtaining complex geometries from a mass production scale perspective in the automotive industry. Since new challenges aiming to reduce CO_2 emissions or increase passenger safety have emerged in recent years, weight reduction has been a primary goal for such industry promoting the introduction of new hot and cold rolled high strength steels and aluminium alloys. To avoid the costly trial and error methods, that are unfortunately still in use, for the correct prediction of forming strategies and their associated relevant phenomena such as springback, cosmetic defects, material behaviour under non-proportional loadings or galling, computational models that are capable of faithfully reproducing their mechanical response, necking and fracture behaviours have to be developed and validated. When it comes to the sheet forming, microstructurally dominated effects such as dynamic strain ageing or paint bake hardening, which are not only restricted to but are generally attributed to aluminium alloys, are particularly troubling for the industry, if an increase of the production rate is anticipated.

* Corresponding author.
E-mail address: berice@mondragon.edu (B. Erice).

https://doi.org/10.1016/j.engfracmech.2023.109471
Received 20 March 2023; Received in revised form 3 July 2023; Accepted 4 July 2023
Available online 7 July 2023

The effect of directionality in the plasticity of aluminium alloys is well understood from a physical point of view and its modelling is no exception. Based on the number of citations, industrial use, and implementation on commercial finite element codes, it seems that the scientific and industrial community mostly converges towards non-quadratic yield functions either based on linear transformations of the stress tensor [1–3], on the generalisation of the stress invariants [4,5] or in higher order polynomials [6–8] as three-dimensional criteria capable of describing the plastic anisotropy of FCC polycrystalline materials and in particular aluminium alloys. In this regard, the former family seems to be more prevalent, and over the years has incorporated three-dimensional extensions of widely used plane stress versions of the Yld2000 [9] or BBC2005 and BBC2008 [10].

As is it the case with the plasticity, ductile fracture as a physical process is also well understood and studied, where the nucleation, growth and coalescence of voids is unanimously accepted by the scientific community as the mechanism responsible. However, its modelling remains as a divisive topic that still generates debate. In this sense, two main currents can be identified: (i) the more academic porous plasticity or GTN models based on the evolution of an internal variable that represents some sort of void volume fraction typically linked to the microstructure [11–13] and (ii) the coupled or uncoupled phenomenological models. From this latter group, we typically refer to those based on a damage mechanics framework that have an internal damage variable that degrades the material as coupled models being Lemaitre's thermodynamically-consistent formulation [14] as one of the most widely used approaches, but are also many others such as [15–17] for example. The uncoupled models are those that can be formulated independently from the constitutive equations and incorporate a damage "indicator", for the lack of a better term, that acts as a quantitative measure indicating how far or close is the fracture from being initiated. On the one hand, these offer the largest degree of flexibility as they can be combined with virtually any continuum plasticity model, usually, they do not suffer from the pathological mesh dependency of the coupled or porous plasticity models, and they are easy to implement in any finite element code. However, they have some other "flaws" or limitations, mainly related to the effect that load non-proportionality has on the formulation, a topic that is discussed at length in [18].

The isotropic uncoupled phenomenological fracture initiation criteria are formulated such that they incorporate the stress state dependency through the modified stress tensor invariants, the stress triaxiality and the Lode angle [19–26] are widely used in the literature and one can attribute their popularity and ubiquitous nature to their potential use in industry. Uncoupled anisotropic criteria are far more uncommon. Most of these are inspired on either stress or strain tensor linear transformations to weigh them and account for the directionality on the fracture. Thus, [27,28] modified the strain tensor calculating a weighted equivalent plastic strain to fracture. [29,30] extended isotropic criteria to anisotropic simply by transforming linearly the stress tensor and reformulating the expressions for the equivalent plastic strain to fracture for proportional loadings. In a similar fashion [31] calculated modified stress invariants from an already linearly transformed stress tensor.

The main objective of this investigation is to analyse and assess the impact that the different stamping speeds can have on the mechanical response and fracture behaviour of a material that is meaningful in a number of common automotive components as is the case of the AA5754 H111 cold rolled sheet, as well as the development of finite element models able to predict such behaviours. The Portevin Le-Chatelier (PLC) effect caused by the dynamic strain ageing has been previously studied and reported for this specific material [32,33]. This effect is clearly observed in the uniaxial tensile tests performed (Fig. 1a), but it is not however the subject of discussion in the current investigation, and it is considered to be far beyond the scope of this work. For more on the PLC modelling aspects and discussion the reader is referred to [34,35]. Preliminary studies were performed to ascertain the approximate strain rates achieved in relevant stamping processes that would correspond to the so-called try out, low and high speed production (3×10^{-3}, 2×10^{-2} and $3\ s^{-1}$) [36]. With this in mind, an extensive experimental campaign that included uniaxial specimens with different geometries machined at different orientations with respect to the Rolling Direction (RD), as well as biaxial specimens at various loading rates aiming towards achieving the afore-mentioned strain rates was performed. Following a hybrid experimental–numerical approach an anisotropic fracture initiation criterion was modified to accommodate the strain rate effects and calibrated for the material studied.

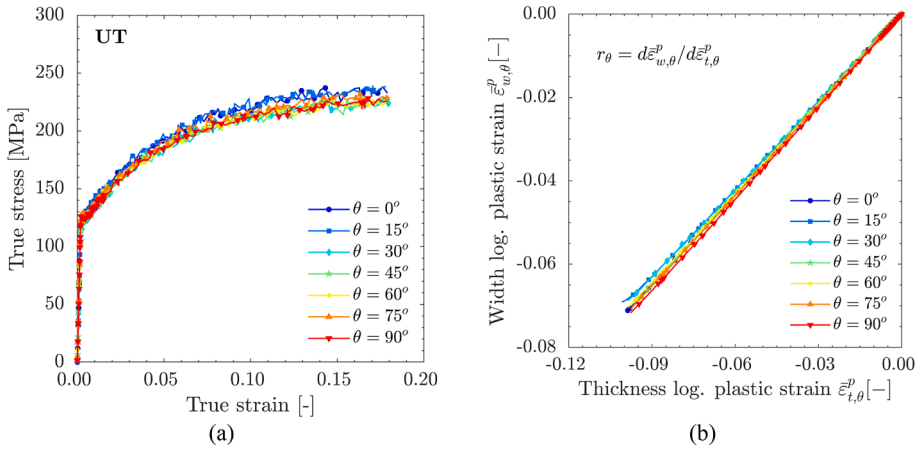

Fig. 1. (a) True stress–strain and (b) Width vs. thickness plastic strain curves of uniaxial tension experiments conducted at different orientations with respect to de RD.

Such approach was also critically analysed and discussed to evaluate its accuracy and validity.

The material description and the different experimental procedures employed for the mechanical testing are included in Section 2. The details of the plasticity constitutive equations and the fracture model as well as an extensive discussion on their predictive capabilities using finite element analysis are given in Sections 3 and 4 respectively.

2. Material and experimental procedures

2.1. Material description

An industrially relevant automotive aluminium alloy (AA5754 H111) has been used for this investigation. The grain distribution analysis performed with an Electron Backscatter Diffraction (EBSD) detector of a Scanning Electron Microscope (SEM) showing light texturing in the RD is depicted in Fig. 2.

2.2. Specimens and experimental procedures

All the specimens were electron discharge machined (wire EDM) from a 1.45 mm AA5754 sheet. Their geometry and dimensions are shown in Fig. 3. The specific use of each one as well as their main features are listed below:

- Uniaxial tension (UT) specimens machined at every 15° up to the Transverse Direction (TD) with respect to the RD were employed to characterise the plasticity. They had a gauge length L_0 of 30 mm and a gauge width of 6 mm.
- 5 mm radius notched tension (NT5) specimens with a minimum gauge width of 10 mm machined in the RD, 45D (45° with respect to the RD) and TD were used to characterise the work hardening and the fracture behaviour of the material.
- 8 mm diameter central hole (CH) specimens with a width of 20 mm, also machined in the RD, 45D and TD were employed for the fracture characterisation.
- In-plane shear (SH) fracture specimens with a 30 mm width were cut in the RD and TD.
- 60 mm length square equibiaxial tension (EBT) specimens were used for the fracture characterisation.

To measure the surface displacements all specimens were spray painted with a black and white speckle pattern and the tests were filmed with two conveniently located 50 mm length objective digital cameras that took images with a resolution of 5 Mpixel for subsequent stereo post-processing with the GOM correlate 2021 commercial stereo digital image correlation (DIC) software. The spatial resolution of the DIC system was 0.019 mm/px, and the subset and step sizes were chosen as 15 px and 5 px respectively.

The NT5, CH and SH specimens were tested in a INSTRON screw-driven universal testing machine equipped with a 50 kN load cell at three different nominal strain rates $\dot{\varepsilon}$ of $2 \times 10^{-4}\ s^{-1}$, $2 \times 10^{-2}\ s^{-1}$ ($2 \times 10^{-3}\ s^{-1}$ CH and SH) and $2 \times 10^{-1}\ s^{-1}$ ($2 \times 10^{-2}\ s^{-1}$ CH and SH), henceforth named as slow, intermediate and fast, where the crosshead velocity was imposed as $v = \dot{\varepsilon} L_0$ for each specimen type, being L_0 the gauge length of the virtual extensometer (marked with red dots in Fig. 3). The UT specimens were only tested under the slow condition.

The EBT specimens were tested in a Erichsen machine [37] equipped with a blank holder of 27 mm of diameter, a 400 kN load cell and a hemispherical punch of 20 mm under quasi-static conditions. The force and displacement of the punch were recorded during the test. The blank holder pushed the specimen against the die applying a force of 10 kN, while the punch moved upwards at a constant velocity of 3 mm/min deforming the specimen until fracture.

2.3. Data processing

Let us consider a Cartesian coordinate system x, y, z in which y is aligned with the axial direction of the tensile specimens. The relative axial displacements ΔL for all the specimens were calculated with the virtual extensometers marked with red dots in Fig. 3. The local axial and transversal total and plastic logarithmic strains were calculated as,

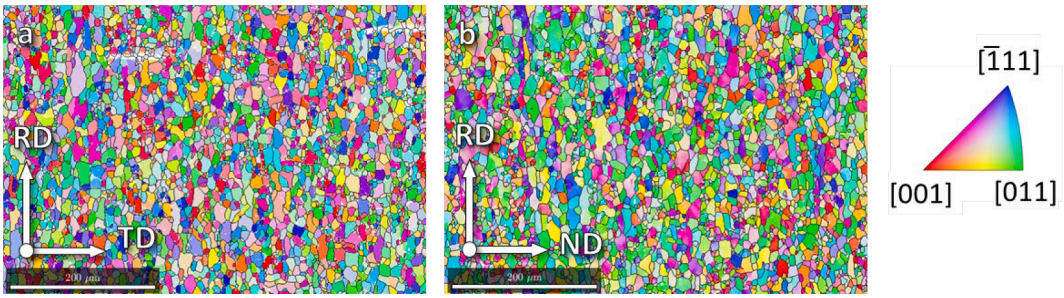

Fig. 2. EBSD orientation maps on RD-TD (a) and RD-ND (b) planes.

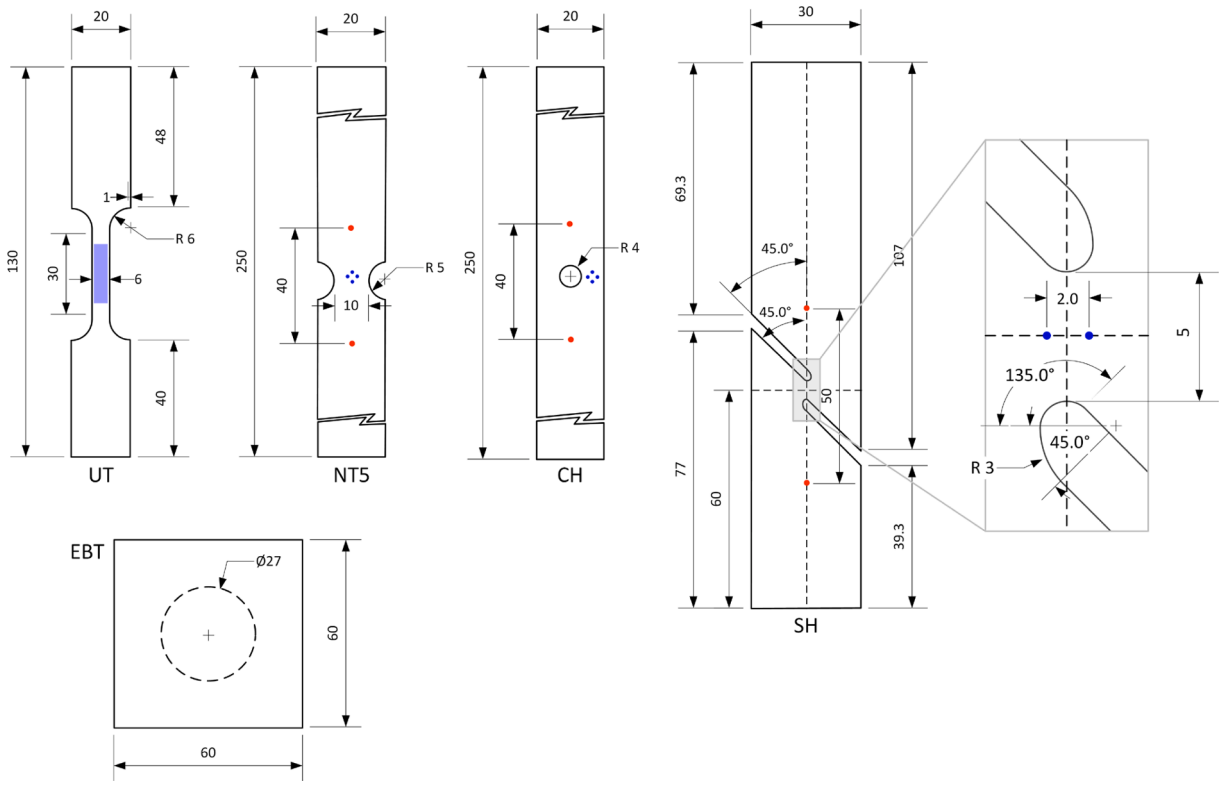

Fig. 3. Dimension and geometries of all the specimens employed in the current study. All dimensions in mm.

$$\varepsilon_{i,\theta} = \ln\left[\Delta l_{i,\theta}/l_o + 1\right] \text{ and } \varepsilon^p_{i,\theta} = \varepsilon_{i,\theta} - \sigma_{ax,\theta}\Big/E, \tag{1}$$

where σ_{ax} is the axial true stress, θ indicates the orientation of the specimen with respect to the RD, E is the elastic modulus and $l_o = 2$ mm is the gauge length of the small virtual extensometers depicted in blue dots in Fig. 3. In the SH specimens the stretch $\lambda = l/l_o$ and angle change of an initially horizontal virtual extensometer were calculated. In the UT specimens identical logarithmic strain measurements were obtained averaging them over the blue area depicted in Fig. 3 or calculating them with the local extensometers.

To quantify the degree of material anisotropy, the directional yield stresses σ_θ (Fig. 4a black dots) and the Lankford coefficients r_θ (Fig. 4a blue dots) were calculated (see Table 1). The former were calculated for the same plastic work per unit volume as that invested in the RD yield stress at 0.01% of plastic strain, whereas the latter were obtained as,

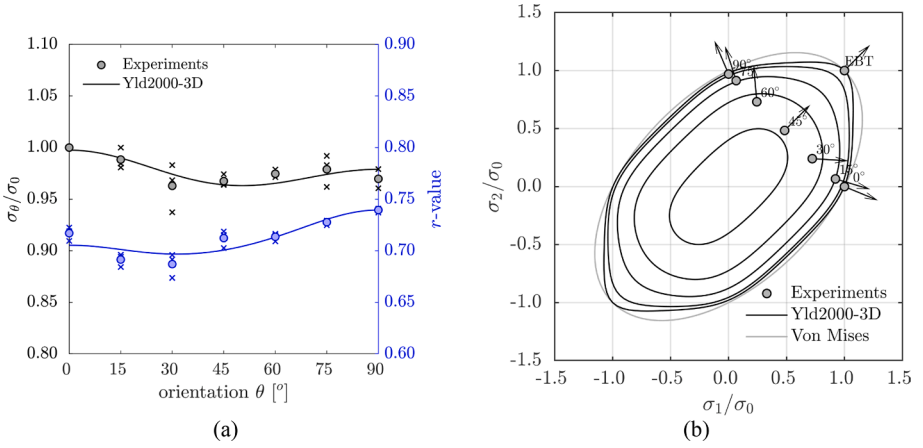

Fig. 4. (a) Experimental vs Yld2000 normalised yield ratios (black) and r-values (blue). (b) Yld2000- 3D plane stress yield surface *iso*-contours for several σ_{12} stresses compared to the von Mises yield surface. (For interpretation of the references to colour in this figure legend, the reader is referred to the web version of this article.)

$$r_\theta = \frac{\dot{\varepsilon}^p_{x,\theta}}{\dot{\varepsilon}^p_{z,\theta}} \tag{2}$$

where $(\dot{\cdot}) = d(\cdot)/dt$ indicates the time derivative of a physical quantity. Please recall that due to plastic incompressibility, $\dot{\varepsilon}^p_{z,\theta} = -\left(\dot{\varepsilon}^p_{x,\theta} + \dot{\varepsilon}^p_{y,\theta}\right)$. The Lankford coefficients can be graphically identifiable as the slope of the $\dot{\varepsilon}^p_{z,\theta} - \dot{\varepsilon}^p_{y,\theta}$ curves as illustrated in Fig. 1b. From here and also from Fig. 4a, it is obvious that the Lankford coefficients are fluctuated around 0.72 regardless of the UT specimen orientation. If we obviate the PLC effect, similar conclusions can be drawn from Fig. 1a and Fig. 4a regarding the anisotropy on the stress–strain response of the material.

3. Anisotropic plasticity modelling

3.1. Constitutive equations

The constitutive equations have been formulated in a corotational or rotationally neutralised configuration where we define the following transformations of the Cauchy stress $\boldsymbol{\Sigma}$ and rate-of-deformation $\boldsymbol{D}$ tensors,

$$\boldsymbol{\sigma} = \mathfrak{R}^T \cdot \boldsymbol{\Sigma} \cdot \mathfrak{R} \text{ and } \boldsymbol{d} = \mathfrak{R}^T \cdot \boldsymbol{D} \cdot \mathfrak{R} \tag{3}$$

where $\mathfrak{R}$ is an orthogonal tensor, i.e. $\mathfrak{R}^{-1} = \mathfrak{R}^T$, that transforms the tensor components between the fixed, global and a corotational, local coordinate systems. The local material coordinate system evolves according to $\dot{\mathfrak{R}} = \boldsymbol{\Omega} \cdot \mathfrak{R}$, where $\boldsymbol{\Omega} = \dot{\boldsymbol{R}} \cdot \boldsymbol{R}^T$ is a spin tensor and $\boldsymbol{R}$ is the rotation tensor coming from the polar decomposition of the deformation gradient $\boldsymbol{F} = \boldsymbol{R} \cdot \boldsymbol{U}$. The rotation tensor, which in this case is $\mathfrak{R} = \boldsymbol{R}$, has an initial value of $\mathfrak{R}|_{t=0} = \boldsymbol{I}$ where $\boldsymbol{I} = \delta_{ij}\boldsymbol{e}_i \otimes \boldsymbol{e}_j$ is the second-order unit tensor.

We assume the additive decomposition of the rate-of-deformation tensor as:

$$\boldsymbol{d} = \boldsymbol{d}^e + \boldsymbol{d}^p \tag{4}$$

where $\boldsymbol{d}^e$ and $\boldsymbol{d}^p$ are the corotational elastic and plastic parts of the rate-of-deformation tensor respectively. The rate form of the linear elastic isotropic law is then defined as:

$$\dot{\boldsymbol{\sigma}} = \mathbb{C} : \boldsymbol{d}^e = \mathbb{C} : (\boldsymbol{d} - \boldsymbol{d}^p) \tag{5}$$

where $\mathbb{C}$ is the isotropic elastic stiffness tensor, a symmetric fourth-order tensor that contains the shear G and the bulk K moduli in the following form:

$$\mathbb{C} = 2G\left\{\mathbb{I} - \frac{1}{3}(\boldsymbol{I} \otimes \boldsymbol{I})\right\} + K\boldsymbol{I} \otimes \boldsymbol{I} \tag{6}$$

G and K are elastic the shear and bulk moduli respectively and $\mathbb{I} = \frac{1}{2}\left(\delta_{ik}\delta_{jl} + \delta_{il}\delta_{jk}\right)\boldsymbol{e}_i \otimes \boldsymbol{e}_j \otimes \boldsymbol{e}_k \otimes \boldsymbol{e}_l$ is the symmetric fourth-order unit tensor.

The three-dimensional extension of the Yld2000-2D yield criterion [38] developed by [9] is used to model the anisotropic flow stress of the material. The Yld2000-3D yield function reads,

$$f\left[\boldsymbol{\sigma}, \bar{\varepsilon}_p, \dot{\bar{\varepsilon}}_p\right] = \bar{\sigma}_a[\boldsymbol{\sigma}] - \sigma_Y\left[\bar{\varepsilon}_p, \dot{\bar{\varepsilon}}_p\right] \tag{7}$$

where σ_Y is the hardening of the material that has the equivalent plastic strain $\bar{\varepsilon}_p = \int \dot{\bar{\varepsilon}}_p dt$, the equivalent plastic strain rate $\dot{\bar{\varepsilon}}_p$ as the internal hardening variables. The anisotropic Yld2000-3D equivalent stress $\bar{\sigma}_a$ is defined as,

Table 1
Material constants for AA5754.

Elastic constants and physical properties								
E[GPa]	ν	$\rho\left[\mathrm{kg/m^3}\right]$	$C_p\left[\frac{\mathrm{J}}{\mathrm{kg^\circ C}}\right]$	$T_m[^\circ\mathrm{C}]$				
70	0.33	2700	900	620				
Yld2000-3D yield function								
α_1	α_2	α_3	α_4	α_5	α_6	α_7	α_8	a
0.946	1.021	0.952	1.020	1.015	0.976	0.999	1.134	8
Swift-Voce strain hardening								
A[MPa]	ε_0	n	σ_0[MPa]	Q[MPa]	B	α	C	$\dot{\varepsilon}_0\left[\mathrm{s^{-1}}\right]$
509.92	1.77×10^{-2}	0.342	127.85	165.00	13.00	0.15	−0.00628	2.0×10^{-4}

$$\overline{\sigma}_a = \left\{ \frac{\phi^{'}[s^{'}] + \phi^{''}[s^{''}]}{2} \right\}^{\frac{1}{a}} \tag{8}$$

where a the is the anisotropic exponent and $\phi^{'}[s^{'}]$ and $\phi^{''}[s^{''}]$ are functions,

$$\phi^{'}[s^{'}] = \left\{ (s^{'}_{11} - s^{'}_{22})^2 + 4\left(s^{'2}_{12} + s^{'2}_{13} + s^{'2}_{23}\right) \right\}^{\frac{a}{2}} \tag{9}$$

$$\begin{aligned} \phi^{''}[s^{''}] = & \left\{ \frac{3}{2}(s^{''}_{11} - s^{''}_{22})^2 + \frac{1}{2}\sqrt{(s^{''}_{11} - s^{''}_{22})^2 + 4(s^{''2}_{12} + s^{''2}_{13} + s^{''2}_{23})} \right\}^a \\ & + \left\{ \frac{3}{2}(s^{''}_{11} - s^{''}_{22})^2 - \frac{1}{2}\sqrt{(s^{''}_{11} - s^{''}_{22})^2 + 4(s^{''2}_{12} + s^{''2}_{13} + s^{''2}_{23})} \right\}^a \end{aligned} \tag{10}$$

that have as arguments the transformed corotational deviatoric stresses $s^{'}$ and $s^{''}$ being $s = \boldsymbol{\sigma} - \frac{1}{3}\mathrm{tr}[\boldsymbol{\sigma}]\boldsymbol{I}$. These are defined through the linear transformations of the corotational Cauchy stress tensor as $s^{'} = L^{'} : \boldsymbol{\sigma}$ and $s^{''} = L^{''} : \boldsymbol{\sigma}$. The $L^{'}$ and $L^{''}$ tensors in their matrix form contain the same eight anisotropic constants, $\alpha_1, .., \alpha_8$ as those defined in the Yld2000 yield function,

$$[L^{'}] = \frac{1}{3}\begin{bmatrix} 2\alpha_1 & -\alpha_1 & -\alpha_1 & 0 & 0 & 0 \\ -\alpha_2 & 2\alpha_2 & -\alpha_2 & 0 & 0 & 0 \\ -2\alpha_1 + \alpha_2 & \alpha_1 - 2\alpha_2 & \alpha_1 + \alpha_2 & 0 & 0 & 0 \\ 0 & 0 & 0 & 3\alpha_7 & 0 & 0 \\ 0 & 0 & 0 & 0 & 3 & 0 \\ 0 & 0 & 0 & 0 & 0 & 3 \end{bmatrix} \tag{11}$$

$$[\mathbb{L}^{''}] = \frac{1}{9}\begin{bmatrix} 2(\alpha_4 - \alpha_3) + 2(4\alpha_5 - \alpha_6) & \alpha_3 - 4(\alpha_4 + \alpha_5 + \alpha_6) & \alpha_3 + 2(\alpha_4 - 2\alpha_5 - \alpha_6) & 0 & 0 & 0 \\ 4(\alpha_3 - \alpha_4 - \alpha_5) + \alpha_6 & 2(4\alpha_4 + \alpha_5 - \alpha_3 - \alpha_6) & 2(\alpha_5 - \alpha_3 - 2\alpha_4) + \alpha_6 & 0 & 0 & 0 \\ 2(\alpha_4 - \alpha_3 - 2\alpha_5) + \alpha_6 & \alpha_3 + 2(\alpha_5 - 2\alpha_4 + 3\alpha_6) & \alpha_3 + \alpha_6 + 2(\alpha_4 + \alpha_5) & 0 & 0 & 0 \\ 0 & 0 & 0 & 9\alpha_8 & 0 & 0 \\ 0 & 0 & 0 & 0 & 9 & 0 \\ 0 & 0 & 0 & 0 & 0 & 9 \end{bmatrix} \tag{12}$$

It should be noted that the yield criterion does collapse into von Mises criterion if $\alpha_1, ..., \alpha_8$ are equal to unity and $a = 2$ only under plane stress conditions.

The work hardening of the material is described with a Swift and Voce strain hardening law, where the strain rate effect is considered to be logarithmic as:

$$\sigma_Y\left[\overline{\varepsilon}_p, \dot{\overline{\varepsilon}}_p\right] = \left(\alpha A\left(\varepsilon_0 + \overline{\varepsilon}_p\right)^n + (1-\alpha)\left\{\sigma_0 + Q\left(1 - \exp\left[-B\overline{\varepsilon}_p\right]\right)\right\}\right)\left(1 + C\ln\left[\frac{\dot{\overline{\varepsilon}}_p}{\dot{\varepsilon}_0}\right]\right) \tag{13}$$

where α is the weighting coefficient, A, ε_0, n and σ_0, Q, B are the Swift and Voce parameters respectively, C is the strain rate coefficient and $\dot{\varepsilon}_0$ is the reference strain rate. Due to the relatively low ranges of strain rates tested, the adiabatic heating was not considered in the current study and thus the thermal softening is not included in the hardening law.

The flow rule is chosen to be associative,

$$\boldsymbol{d}^p = \dot{\lambda}\frac{\partial f}{\partial \boldsymbol{\sigma}} = \dot{\lambda}\boldsymbol{n} \tag{14}$$

where λ is the plastic multiplier. Operating on the work conjugacy, i.e., $\boldsymbol{\sigma} : \boldsymbol{d}^p = \overline{\sigma}_a\dot{\overline{\varepsilon}}_p$, one gets the evolution equation as $\dot{\overline{\varepsilon}}_p = \dot{\lambda}$ being $\overline{\varepsilon}_p = \int \dot{\overline{\varepsilon}}_p dt$. Thus, using Euler's theorem for first order homogeneous functions, such as the equivalent stress, $\overline{\sigma}_a[\boldsymbol{\sigma}] = \boldsymbol{\sigma} : \boldsymbol{n}$. The loading/unloading conditions are stated in Kuhn-Tucker form as:

$$f \leqslant 0, \dot{\lambda} \geqslant 0, \dot{\lambda} f = 0 \tag{15}$$

The plastic multiplier is determined algorithmically from the linearised consistency condition using the Wang or consistency model [39] and the discretized from of the constitutive equations. The constitutive model equations were implemented in their incremental form as a user defined material subroutine in ABAQUS/Explicit [40] non-linear explicit time integration FE solver.

Table 2
Averaged values over strains of 2%, 4% and 6%.

σ_0/σ_0	σ_{15}/σ_0	σ_{30}/σ_0	σ_{45}/σ_0	σ_{60}/σ_0	σ_{75}/σ_0	σ_{90}/σ_0	σ_{EBT}/σ_0
1.000	0.988	0.963	0.967	0.975	0.979	0.969	1.000
r_0	r_{15}	r_{30}	r_{45}	r_{60}	r_{75}	r_{90}	r_{EBT}
0.723	0.697	0.703	0.726	0.718	0.728	0.739	1.000

3.2. Parameter identification

The yield function constants $\alpha_1,..,\alpha_8$, were directly calibrated using the experimental data from the UT and EBT tests in the same fashion as for the original Yld2000 yield function [9] (see Table 2). The constants were calibrated by minimising the following cost function:

$$\mathscr{E} = \sum_{i=\mathrm{UT}_\theta}\left(\frac{\overline{\sigma}_a[\boldsymbol{\sigma}_\theta]}{\sigma_\theta^{\exp}}-1\right)^2 + \sum_{i=\mathrm{EBT}}\left(\frac{\overline{\sigma}_a[\boldsymbol{\sigma}_{\mathrm{EBT}}]}{\sigma_{\mathrm{EBT}}^{\exp}}-1\right)^2 + \sum_{i=\mathrm{UT}_\theta}\left(\frac{r_\theta}{r_\theta^{\exp}}-1\right)^2 + \sum_{i=\mathrm{EBT}}\left(\frac{r_{EBT}}{r_{\mathrm{EBT}}^{\exp}}-1\right)^2 \tag{16}$$

where the plane stress tensors for the UT and EBT specimens are,

$$\boldsymbol{\sigma}_\theta = \sigma_0\left\{\cos^2[\theta]\boldsymbol{e}_1\otimes\boldsymbol{e}_1 + \sin^2[\theta]\boldsymbol{e}_2\otimes\boldsymbol{e}_2 + 2\sin[\theta]\cos[\theta](\boldsymbol{e}_1\otimes\boldsymbol{e}_2)^S\right\} \tag{17}$$

and

$$\boldsymbol{\sigma}_{\mathrm{EBT}} = \sigma_0(\boldsymbol{e}_1\otimes\boldsymbol{e}_1 + \boldsymbol{e}_2\otimes\boldsymbol{e}_2) \tag{18}$$

In this particular case, since there was no direct measurement of the equibiaxial yield stress, $\sigma_{\mathrm{EBT}}^{\exp} = \sigma_0$ has been chosen. This value should be checked, simulating the EBT experiment at least against the experimental force–displacement and assess if such approximation is indeed valid (see subsequent subsection).

The predictions of the model (solid lines) were compared against the average (marked with dots) of three experimental datapoints (marked with crosses) in Fig. 4, where the black coloured data are the normalised directional yield stresses, and the blue data are the r-values. Fig. 4b shows the plane stress yield surface for different values of σ_{12} stresses shown as contours with the experimental yield stresses on top. The corresponding von Mises yield surface has been added for comparison purposes.

3.3. Numerical simulations

The same numerical setup was employed to simulate all the tensile numerical simulations, which included the virtual testing of NT5, CH and SH specimens. The symmetry conditions of all specimens were exploited, using one-eight of the geometry for the NT5 and CH specimens and mid-plane half symmetry in the case of the SH. The geometries were discretised with eight C3D8R linear solid eight-node reduced-integration elements with hourglass control over half thickness that had a face area of 0.1×0.1 mm^2 in the zones where the plastic strains were localised, as shown in Fig. 5. The velocity histories measured with DIC during the experiments were applied as boundary conditions in a mass scaled solution that used 10^5 increments over the total calculation time giving a ratio of internal to kinetic energy of more than five orders of magnitude.

To identify the work hardening constants numerical simulations of the RD (θ=0°) NT5 specimens were carried out with the domain reduction iterative inverse modelling procedure available in the LS-OPT commercial software was employed. The sum of the minimum square error of the experimental versus finite element simulation (see Fig. 6) force–displacement, and local axial and transversal logarithmic strain–displacement curves were used as the cost function. The simulations performed with the identified constants were in excellent agreement with the experimental data as shown in Fig. 6a and c.

One-fourth of the EBT specimen was discretised, whereas the die and the punch were modelled as rigid surfaces. The clamping of the specimen by the blank holder was simulated by fixing the degrees of freedom of the outer edge nodes (see Fig. 5). The geometry and dimensions of these components were as listed in the ISO standard [37]. A friction coefficient of 0.05 between the sheet and the punch, while a value of 0.2 was set for rest of the components in the penalty contact algorithm. The displacement of the punch was prescribed with the velocity history measured in the tests.

The global (force–displacement) and local (logarithmic strains-displacement) behaviours were in very good agreement with the slow experiments for all the orientations (Fig. 6a, b and c). In the$\theta = 45°$ NT5 simulations, however, the transversal local logarithmic

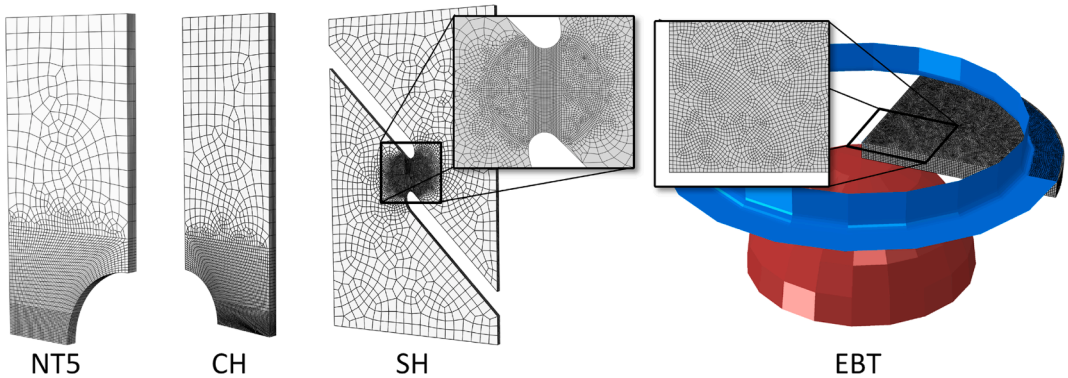

Fig. 5. Finite element meshes of the fracture specimens.

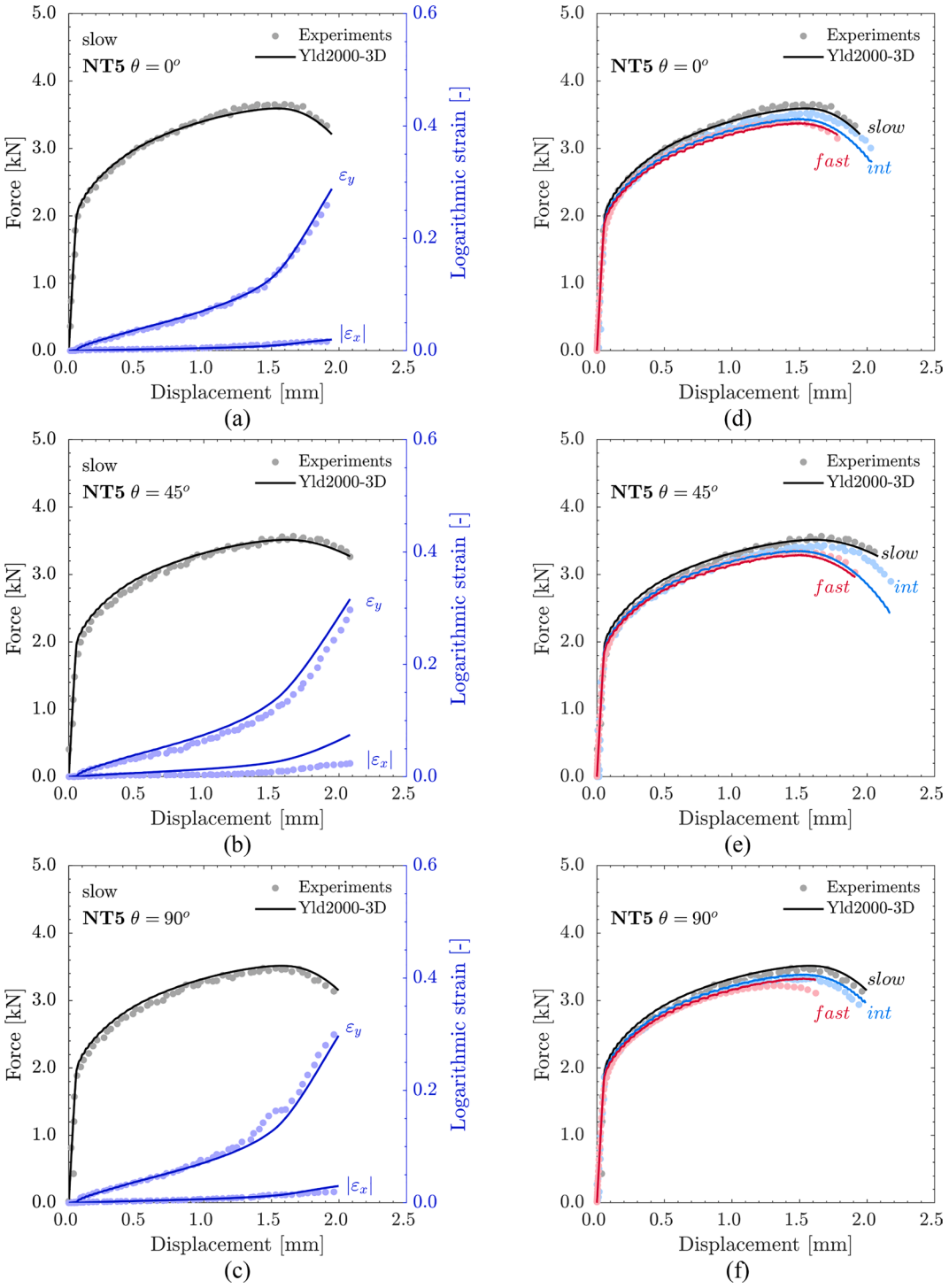

Fig. 6. (a-c) Numerical vs. experimental force–displacement and local logarithmic strains-displacement curves of the NT5 specimens, as well as force–displacement curves at several strain rates (d-f).

strain was not properly captured by the model as illustrated in Fig. 6b. With the exception of the force–displacement curves for intermediate$\theta = 45^\circ$ and fast$\theta = 90^\circ$ that were underestimated and overestimated respectively (see Fig. 6e and f), the overall response was very well described by a simple Johnson-Cook negative strain rate hardening law, as shown in Fig. 6d, e and f.

In general, the slow CH simulations follow the same trends as those of the NT5, that is, good agreement in$\theta = 0^\circ$ and$\theta = 90^\circ$ orientations showing less than a 2% difference in the force and local axial strains, (see Fig. 7a and b) but differences at$\theta = 45^\circ$ (Fig. 7c).

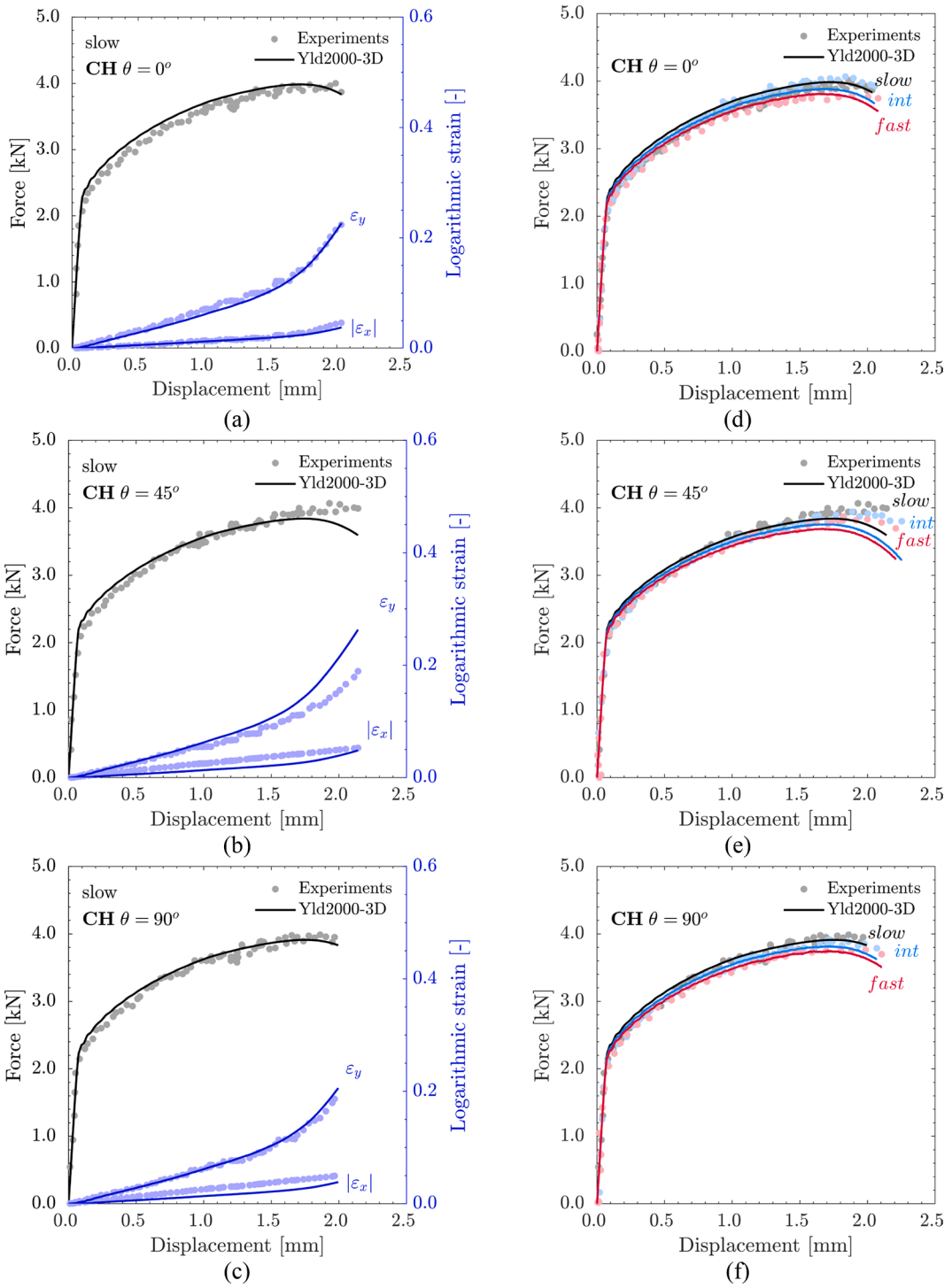

Fig. 7. (a-c) Numerical vs. experimental force–displacement and local logarithmic strains-displacement curves of the CH specimens, as well as force–displacement curves at several strain rates (d-f).

However, in the latter case the model seemed to accumulate plastic strain earlier than in the experiment, which translated into an early neck, hence showing differences at the onset of fracture of 14% and 35% in the force–displacement and local axial strain. This was observed in all three loading rates as depicted in Fig. 7e. The model gave good force–displacement response predictions (differences of less than 6%) for the intermediate and fast loading rates for the other orientations as shown in Fig. 7d and f.

Both global and local mechanical responses were faithfully predicted (see Fig. 8a and b) by the model in the simulations of the RD

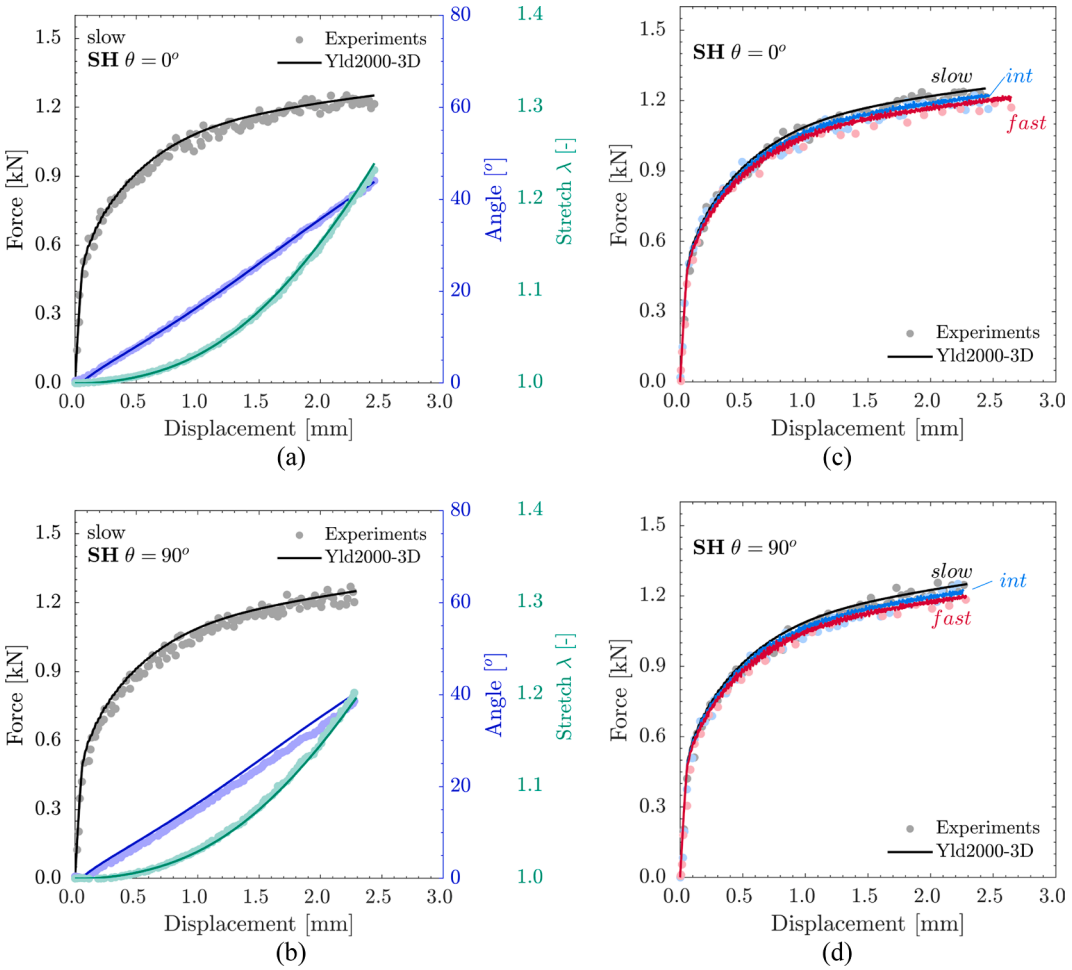

Fig. 8. (a-b) Numerical vs. experimental force–displacement, local extensometer stretch-displacement and rotation angle-displacement curves of the SH specimens, as well as force–displacement curves at several strain rates (c-d).

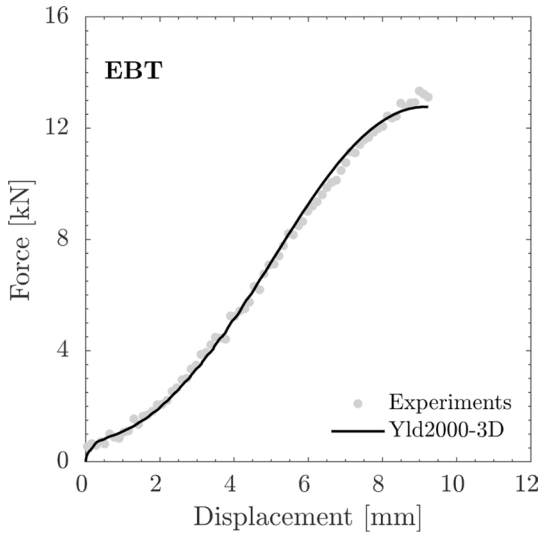

Fig. 9. Numerical vs. experimental force–displacement curve of the EBT specimen.

and TD SH specimens at the three loading rates (see Fig. 8c and d). Although the model was not able to perfectly capture the experimentally observed behaviour at $\theta = 45^{\circ}$ for the NT5 and CH specimens, which could be potentially attributed initially to a unsuitable choice of the $\sigma_{\mathrm{EBT}}^{\mathrm{exp}}$ estimation, the EBT simulations were in excellent agreement with the experimentally measured force–displacement curve, as it can be seen in Fig. 9.

Granting that in all the previously-mentioned plots the experimental data are depicted with points, if carefully observed, the PLC effect is clearly present in all of them to a greater or lesser extent. As it has been stated in the introduction, we have considered this effect to fall out of scope of the current investigation. Nevertheless, it can help to understand some of the "irregularities" observed in the experiments, as for example the serrations in the force or the sudden smooth to "staircase" transitions in the strains due to the elastic unloadings after the plastic bands have travelled inside the specimens (see Fig. 6c and Fig. 7b) (Table 2).

4. Anisotropic fracture

4.1. Anisotropic fracture initiation criterion

The stress state of an isotropic material can be characterised by the principal stress ratios σ_I/σ_{II} and σ_{II}/σ_{III} being $\sigma_I \geqslant \sigma_{II} \geqslant \sigma_{III}$ or alternatively using the stress triaxiality η and the Lode angle parameter $\bar{\theta}$,

$$\eta = \frac{\mathrm{tr}[\boldsymbol{\sigma}]}{\bar{\sigma}}, \bar{\theta} = 1 - \frac{2}{\pi}\mathrm{acos}\left[\frac{27}{2}\frac{\det[\boldsymbol{s}]}{\bar{\sigma}^3}\right] \tag{19}$$

where $\bar{\sigma} = \sqrt{\frac{3}{2}\boldsymbol{s} : \boldsymbol{s}}$ is the von Mises equivalent stress.

The isotropic Hosford-Coulomb criterion for proportional loadings gives an explicit expression for the equivalent plastic strain to fracture as a function of the stress-state as:

$$\bar{\varepsilon}_f^{pr}[\eta, \bar{\theta}] = b\left(\frac{1+c}{g[\eta, \bar{\theta}]}\right)^{\frac{1}{n}} \tag{20}$$

with the stress-state-dependent function $g[\eta, \bar{\theta}]$ defined as follows,

$$g[\eta, \bar{\theta}] = \left\{\frac{1}{2}\left(|f_1[\bar{\theta}] - f_2[\bar{\theta}]|^a + |f_2[\bar{\theta}] - f_3[\bar{\theta}]|^a + |f_1[\bar{\theta}] - f_3[\bar{\theta}]|^a\right)\right\}^{\frac{1}{a}} + c(2\eta + f_1[\bar{\theta}] + f_3[\bar{\theta}]) \tag{21}$$

where a, b, c and n are the fracture material constants with the following Lode parameter dependent algebraic functions:
$f_1[\bar{\theta}] = \frac{2}{3}\cos\left[\frac{\pi}{6}(1-\bar{\theta})\right]$, $f_2[\bar{\theta}] = \frac{2}{3}\cos\left[\frac{\pi}{6}(3+\bar{\theta})\right]$ and $f_3[\bar{\theta}] = -\frac{2}{3}\cos\left[\frac{\pi}{6}(1+\bar{\theta})\right]$ (22).
To account for the non-proportional loadings, a damage indicator D is defined in integral form,

$$D = \int_0^{\bar{\varepsilon}_p^f} \frac{d\bar{\varepsilon}_p}{\bar{\varepsilon}_f^{pr}[\eta, \bar{\theta}]} \tag{23}$$

where $\bar{\varepsilon}_f^{pr}[\eta, \bar{\theta}]$ is a function of the loading history of the material, i.e. $\{\eta[t], \bar{\theta}[t]\}$. Although the authors are well aware of the limitations of this type of phenomenological uncoupled fracture initiation criteria, as discussed in [18], the excellent results provided by these and their sustained use more than three decades in the industry are still strong motives for their further development.

In the anisotropic case, one can define the stress state with five Cauchy stress tensor components if it is normalised by the von Mises stress as $\boldsymbol{\sigma}/\bar{\sigma}$ [29]. To account for the fracture anisotropy linear stress transformations are used such that $\tilde{\boldsymbol{\sigma}} = \mathbb{M} : \boldsymbol{\sigma}$, where $\mathbb{M}$ is a fourth order tensor that contains the weighing parameters. In this particular case, $\mathbb{M}$ has the following matrix form,

$$[\mathbb{M}] = \begin{bmatrix} 1 & m_{12} & 0 & 0 & 0 & 0 \\ 0 & m_{22} & 0 & 0 & 0 & 0 \\ 0 & 0 & 1 & 0 & 0 & 0 \\ 0 & 0 & 0 & m_{44} & 0 & 0 \\ 0 & 0 & 0 & 0 & 1 & 0 \\ 0 & 0 & 0 & 0 & 0 & 1 \end{bmatrix} \tag{24}$$

being m_{12}, m_{22} and m_{44} the weighing constants. Again, the non-proportionality is accounted for reformulating the damage indicator as,

$$D = \int_0^{\bar{\varepsilon}_p^f} \frac{d\bar{\varepsilon}_p}{\bar{\varepsilon}_f^{pr}[\tilde{\boldsymbol{\sigma}}/\bar{\sigma}]} = 1 \text{ with } \bar{\varepsilon}_f^{pr}[\tilde{\boldsymbol{\sigma}}/\bar{\sigma}] = b\left(\frac{1+c}{g[\tilde{\boldsymbol{\sigma}}/\bar{\sigma}]}\right)^{\frac{1}{n}}, \tag{25}$$

where $g[\tilde{\boldsymbol{\sigma}}/\bar{\sigma}]$ has the same form as in Equation (21).

4.2. Constant identification

The set of constants $\boldsymbol{k} = \{a, b, c, n, m_{12}, m_{22}, m_{44}\}$, of the anisotropic Hosford-Coulomb fracture initiation criterion were obtained minimising the following cost function:

$$\mathscr{E}[\boldsymbol{k}] = \max_{i}^{N} \left[\left| \frac{\overline{\varepsilon}_{f,i,\theta}\left[\boldsymbol{\sigma}^{\text{num}}_{f,i,\theta}, \boldsymbol{k}\right]}{\overline{\varepsilon}^{\text{num}}_{f,i,\theta}} - 1 \right| \right] \tag{26}$$

where $\overline{\varepsilon}^{\text{num}}_{f,i}$ is the equivalent plastic strain gathered from the critical element at the onset of fracture detected in each one of the specimens $i = \{\text{NT5}, \text{CH}, \text{SH}, \text{EBT}\}$ oriented at an angle θ with respect to the RD and $\overline{\varepsilon}_{f,i}$ is obtained from the integration of the damage indicator over the non-proportional loading paths characterised by the stress histories $\boldsymbol{\sigma}^{\text{num}}_{f,i,\theta}$ (see Table 3). The critical elements were considered as those with the largest equivalent plastic strain when the experimental displacement at the onset of fracture was attained in the simulations. The equivalent plastic strain of the NT5 and CH centreline elements are plotted from the centres to the edges of the specimens for the time corresponding to the onset of fracture in Fig. 10 and Fig. 11 respectively. The figures clearly show the location of the largest plastic strains as well as the distribution of those across the width of the specimen, making easier the identification with a quick visual inspection. In the case of the SH specimens, the largest strains were detected on the surface rather than in the midplane, therefore all the integration points of the surface gauge area are shown in Fig. 12 for the time corresponding to the onset fracture. The DIC analysis of such specimens, shown in Fig. 12, gave similar results as those by the, confirming that the local strain fields were captured by the constitutive model. Please note that the contours are shown in equivalent von Mises strain ($\dot{\bar{\varepsilon}} = \sqrt{\frac{2}{3}\boldsymbol{d}^p : \boldsymbol{d}^p}$), rather than in equivalent plastic strains. However, minor deviations are expected from this assumption, since the elastic strains are almost negligible and the differences between the equivalent and von Mises strains are also very small [41].

From the DIC analysis and the post-mortem specimen inspection (see Fig. 13a) the fracture in the EBT run along the TD direction. The critical element in this case, was considered as that which integration point was located along the TD and had the largest equivalent plastic strain, marked with a circle in Fig. 13b. Although larger, as shown in the contours corresponding to the onset of fracture in Fig. 13b, the RD plastic strain difference with that of the TD is extremely small, down to the fourth decimal. However, the suitability of all the selected elements for the different specimen types will be further discussed in subsequent sections (Table 1).

4.3. Loading paths to fracture

As the stress state is characterised by the stress tensor components instead of the isotropic magnitudes, such as the triaxiality and Lode parameters, the strain paths to fracture are challenging to visualise. Following the ideas exposed in [29], two polar plots are constructed to depict the anisotropic effect on the loading paths.

- The $\{\sigma_{11}, \sigma_{22}\}$ biaxial plane where the paths have an argument $r = \overline{\varepsilon}_p$ and an angle $\varphi = \text{atan}[\sigma_{22}/\sigma_{11}]$, which give an abscissa of $x = \overline{\varepsilon}_p \cos[\varphi] = \overline{\varepsilon}_p \sigma_{11}/\sqrt{\sigma_{11}^2 + \sigma_{22}^2}$ and an ordinate $y = \overline{\varepsilon}_p \sin[\varphi] = \overline{\varepsilon}_p \sigma_{22}/\sqrt{\sigma_{11}^2 + \sigma_{22}^2}$ in Cartesian coordinates as illustrated in a Fig. 14a. This plane will contain the paths of the specimens that mostly are under biaxial stress states. For guidance purposes, auxiliary lines showing proportional loadings for the isotropic cases of uniaxial ($\eta = 1/3, \sigma_{22}/\sigma_{11} = 0$), biaxial ($\eta = 2/3, \sigma_{22}/\sigma_{11} = 1$) and plane strain tension $\eta = 2/3, \sigma_{12}/\sigma_d = \sqrt{2}/6$ ($\eta = 1/\sqrt{3}, \sigma_{22}/\sigma_{11} = 1/2$) as well as shear ($\eta = 0, \sigma_{22}/\sigma_{11} = -1$) are plotted.
- The $\{\sigma_{12}, \sigma_d\}$ plane that contains the paths with same argument and the angle $\theta = \text{atan}[\sigma_{12}/\sigma_d]$ with an abscissa of $x = \overline{\varepsilon}_p \cos[\theta] = \overline{\varepsilon}_p \sigma_d/\sqrt{\sigma_{12}^2 + \sigma_d^2}$ and an ordinate of $y = \overline{\varepsilon}_p \sin[\theta] = \overline{\varepsilon}_p \sigma_{12}/\sqrt{\sigma_{12}^2 + \sigma_d^2}$ in Cartesian coordinates. This plane is used to plot the loading paths that exhibit a stress states that mostly have $\sigma_{11} \simeq \sigma_{22}$ and a shear component σ_{12} as is the case for the specimens oriented at 45° from the RD, hence $\sigma_d = \sqrt{2}\sigma_{11} = \sqrt{2}\sigma_{22}$. Again, auxiliary lines are plotted for the uniaxial ($\eta = 1/3, \sigma_{12}/\sigma_d = \sqrt{2}/2$), biaxial ($\eta = 2/3, \sigma_{12}/\sigma_d = 0$) and plane strain tension ($\eta = 1/\sqrt{3}, \sigma_{12}/\sigma_d = \sqrt{2}/6$) isotropic cases as a guidance (see Fig. 14b)

All the NT5 (blue), CH (red) and EBT (green) specimen loading paths are shown in the first quadrant, biaxial tension, of Fig. 14c, while the RD and TD SH (teal) specimens are plotted in the second and fourth quadrant respectively. The EBT and 45° oriented specimens were contained in the equibiaxial plane. The plot shows the depart from isotropic fracture, losing the symmetry with respect to the line corresponding to the equibiaxial stress state. Although one could argue that the differences in such symmetry are not that large, in the case of the NT5 specimens, the critical element location varied depending on their orientation as shown in Fig. 10a. The loading paths on the $\{\sigma_{12}, \sigma_d\}$ plane include all the specimens oriented at 45° and the EBT. Although the SH specimens depart from

Table 3
Anisotropic Hosford-Coulomb fracture initiation constants for the AA5754 under quasi-static loading conditions, nominally at a strain rate of 2×10^{-4} s^{-1}.

a	b	c	n	m_{12}	m_{22}	m_{44}
0.8321	1.1530	0.1383	0.2480	−0.1176	1.0748	1.1465

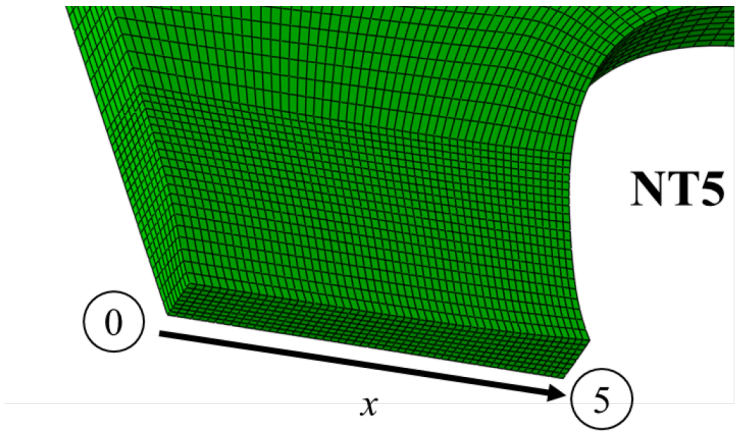

(a)

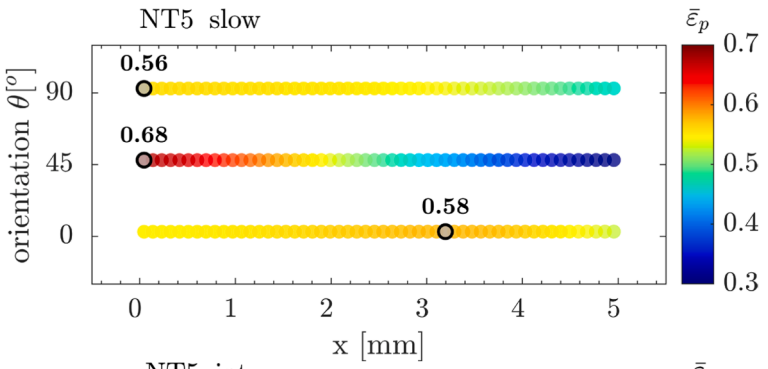

(b)

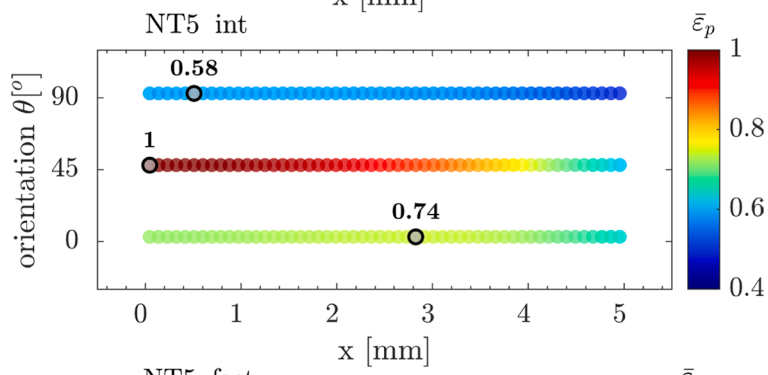

(c)

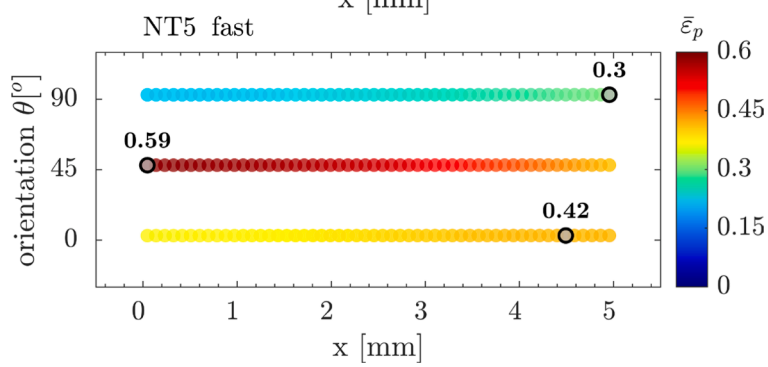

Fig. 10. Equivalent plastic strain of the elements located in the midplane centreline across the width of the NT5 specimen simulations at the onset of fracture. The maximum equivalent plastic strain location is indicated with a with a circle along with its value.

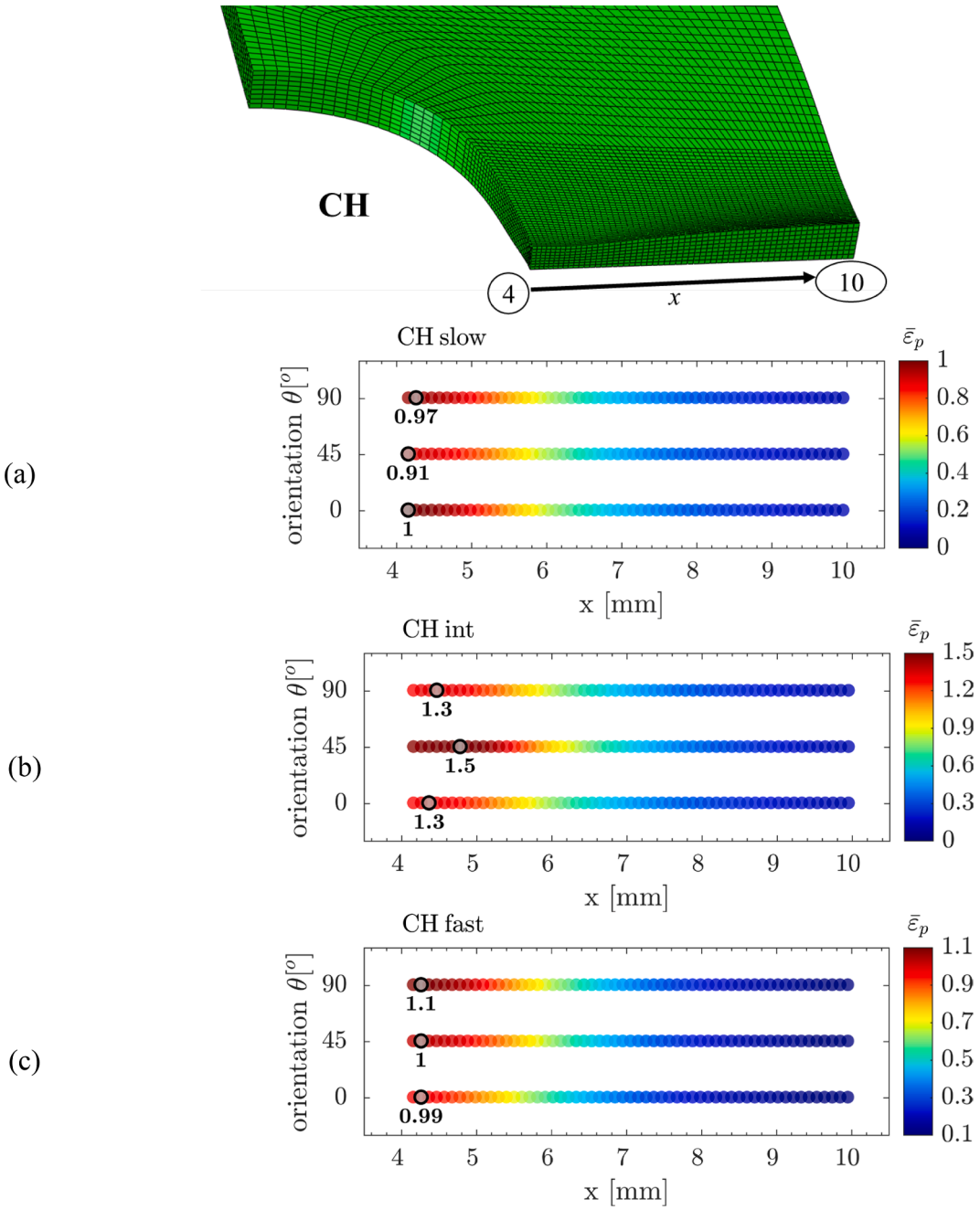

Fig. 11. Equivalent plastic strain of the elements located in the midplane centreline across the width of the CH specimen simulations at the onset of fracture. The maximum equivalent plastic strain location is indicated with a with a circle along with its value.

their ideal stress state, i.e. contained in the shear plane ($\sigma_{11} \simeq -\sigma_{22}$ or $\sigma_{11} \simeq -\sigma_{22}$), it was decided to also plot them with the former as they also had shear stress components.

4.4. Fracture initiation point

One of the most controversial and widely used procedures to calibrate phenomenological fracture initiation criteria, such as that used in this investigation, is the selection of the so-called critical element. As explained in previous subsections, the whole procedure relies on the stress tensor and equivalent plastic strain histories being collected from the element that it is considered to fail first. A reasonable choice, followed by many authors [42–46], is to locate the element with the largest equivalent plastic strain at the onset of

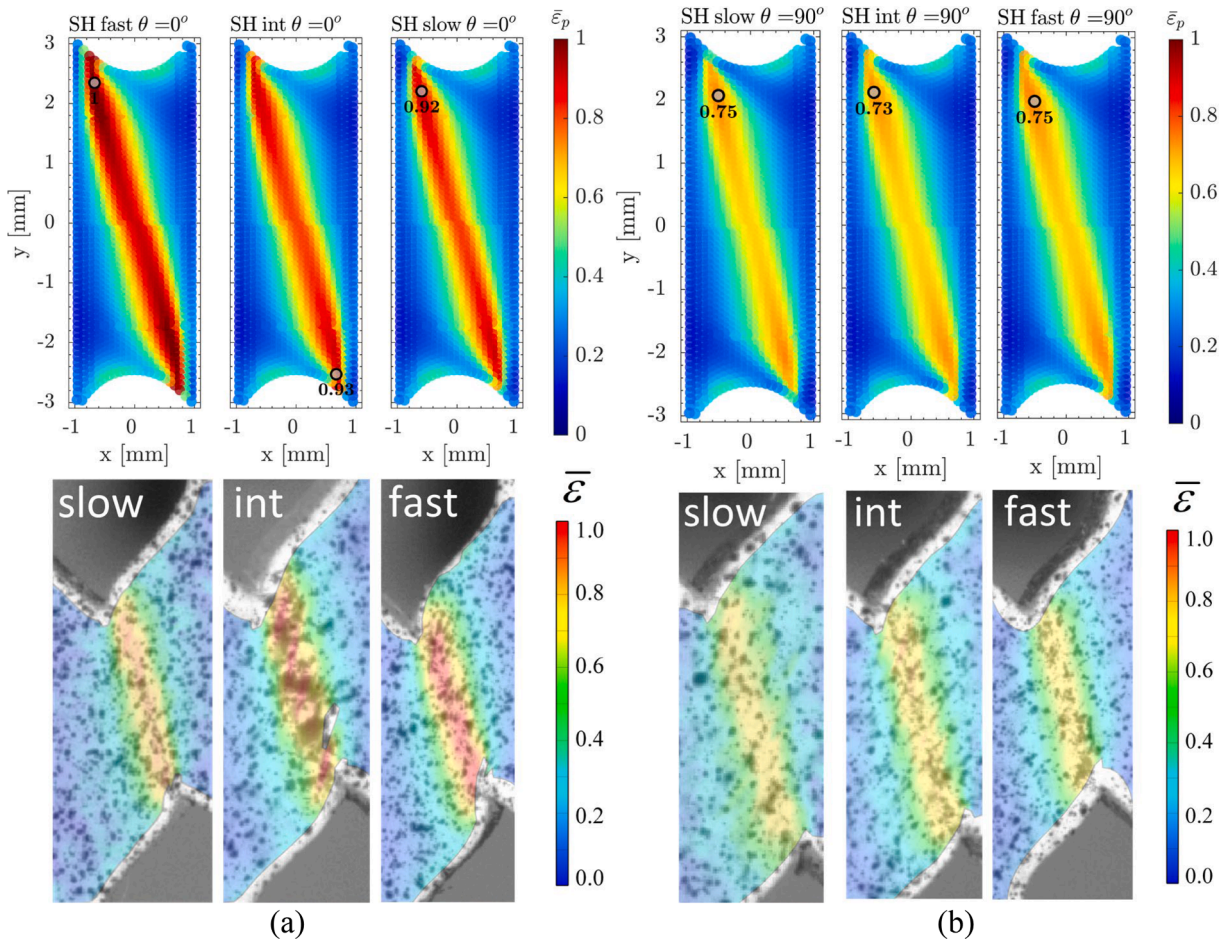

Fig. 12. Equivalent plastic strain of the elements located on the surface of the gauge area from the RD (a) and TD (b) SH specimen simulations (top) and DIC analysis (bottom) at the onset of fracture. The maximum equivalent plastic strain location is indicated with a with a circle along with its value.

fracture. However, as an integral form of the damage indicator is utilised in this particular case, such an indicator is dependent on the behaviour in a particular region of the mesh – where the indicator may be fully saturated before the area with the largest plastic strain. This would lead to incorrect fracture predictions. It is therefore important to estimate how close or distant are the elements with the largest equivalent plastic strain versus those with the highest damage indicator. To avoid any further confusion, the former will be referred as the critical element or point, whereas the latter will be referred as the fracture initiation point.

Analysing the tensile specimens, i.e. NT5, CH and SH, to visually pin point the fracture initiation point is extremely challenging. Some have used Scanning Electron Microscope images of notched specimens to roughly locate fracture initiation on post-mortem fracture surfaces as in [47]. However, for shear specimens becomes even more challenging. Here, we decided to make use of the stress tensor component and equivalent plastic strain histories collected from the simulations to compute the damage indicator with the already calibrated fracture criterion constants. If unity was reached at any of the points, then the simulation was stopped and the locations of the critical and fracture initiation points were plotted with their corresponding damage indicator values. If the damage indicator did not reach unity, then the maximum values attained at the onset of fracture displacement were compared. Note that we refer to the onset of fracture displacement as that detected experimentally from the force–displacement curves.

From Fig. 10a, we can see that the RD NT5 had a significant notch effect, smearing the largest plastic strains in a small area close to the notch root. The plastic strains are not still concentrated in the centre of the specimen as occurs for larger deformations, e.g. the specimens with orientations at 45° and 90°. A small discrepancy (less than 5%) between the fracture initiation and critical point locations were found. The damage indicator values corresponding to both points were still very close nonetheless, 0.96 for the critical point (see Fig. 15b). The fracture criterion predicted failure almost 1 mm away from the critical element towards the centre. As mentioned before, the plastic strains were concentrated in the centre for the rest of the specimens, which came as a result of necks developing in this location, and consequently the fracture initiation point coincided with the centre itself. Overall, even if slight deviations were encountered for the RD specimen, it did not have much effect in the force–displacement curve as shown in Fig. 15a, where the critical and fracture initiation points are marked with a circle and a diamond respectively.

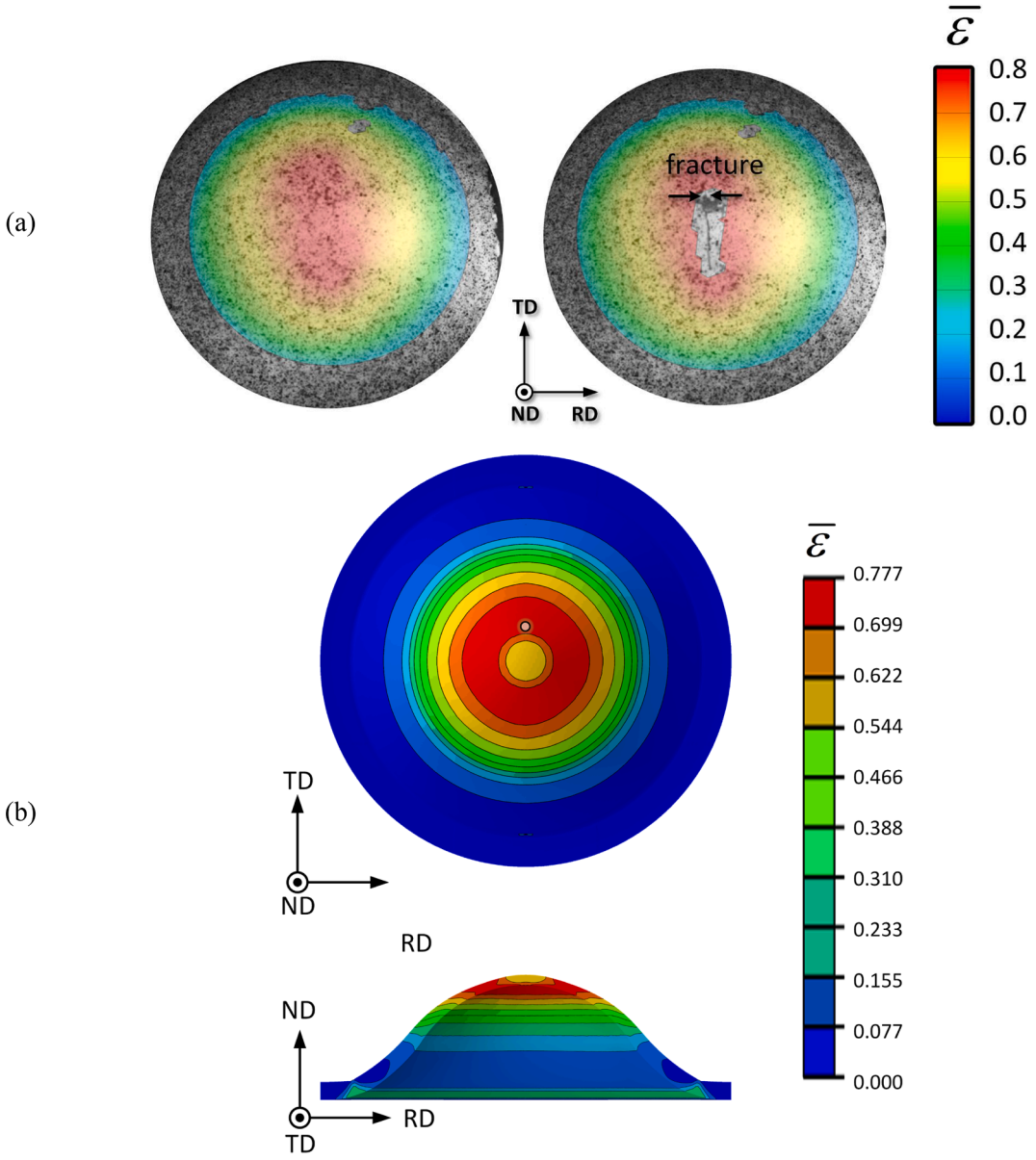

Fig. 13. (a) Equivalent von Mises strain contours on the surface of a EBT specimen computed from the DIC analysis. (b) Equivalent von Mises strain contours of the finite element simulations of EBT specimens, where the maximum equivalent plastic strain location is marked with a with a circle.

In general, for all orientations, the largest equivalent plastic strain location in the CH specimens prior to incipient necking was located very close to the hole edge and moved away from it as the specimen was deformed and necking was fully formed. Noting that the necking on these type of specimen geometries always develops at a certain distance from the hole edge [48]. From Fig. 15d, it is clear that the critical points were almost, if not right at the hole edge. The fracture model however, for the specimens oriented at 0° and 45° predicted failure roughly 1 mm away from such location, where an incipient neck was later developed in the simulations. Other than in the TD CH, we can conclude that the fracture initiation point, according to the model, was located away from the hole edge and close from where the neck developed as depicted in Fig. 15d. Again, as in the case of the NT5 specimens, the displacements corresponding to the fracture initiation and critical points were not that far apart (see Fig. 15c). The largest difference in terms of displacement, around 0.12 mm, was detected for the RD CH.

The location of the fracture initiation and critical points in the TD SH specimen were identical, while for the RD specimen were slightly different as it can be observed in Fig. 16b. The latter difference, although small, was also translated in a premature fracture displacement prediction, being the critical and fracture initiation points 0.12 mm apart, as shown in Fig. 16a. As pointed out in previous subsections and according to the numerical simulations, the areas with larger equivalent plastic strains were located on the surface of the specimens. In theory, this could allow for a relatively easy visual inspection of the image sequences captured during the

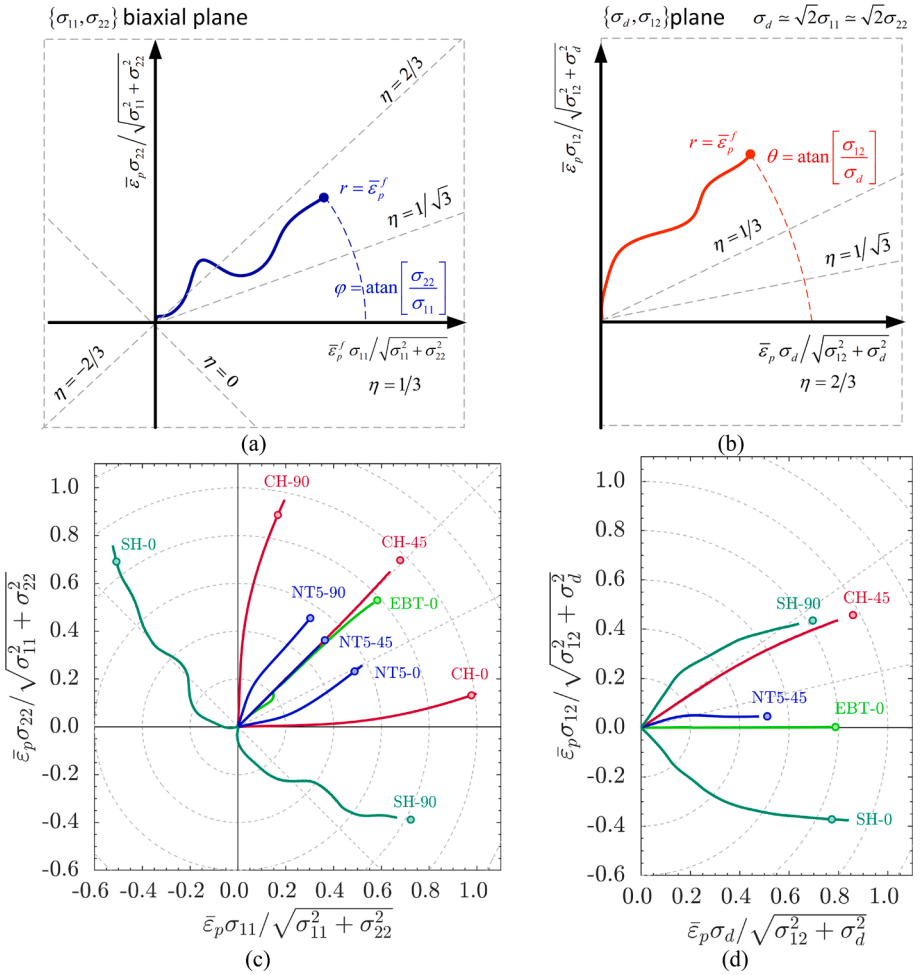

Fig. 14. (a-b) Schematic polar plot diagrams for the depiction of the loading paths to fracture. (c-d) Loading paths to fracture of the specimens under quasi-static loading conditions. The fracture initiation criterion's predictions are marked with circles.

tests correlating the crack formation with the fracture initiation point. Fig. 16c shows DIC analysed images depicting von Mises strain contours corresponding to the displacements marked in circled numbers in Fig. 16a (force–displacement curve of the slow RD SH). From this set of images is extremely challenging to visually identify the fracture initiation. The fracture process is clearly taking place from points ③(the force starts dropping) to ④(the force drops catastrophically). The bottom part of Fig. 16c illustrates this sequence, in which the sheared area has been highlighted. In here, the transition from initiation to the fully formed shear crack can be observed. From these however, it is extremely challenging to firmly establish weather the crack initiates from the edges or somewhere inside the gauge area of the highlighted shear zone.

The critical point in the EBT specimen, on the top surface located along the TD, coincided with the fracture initiation point predicted by the model. The damage contours shown in Fig. 17b helped to visually confirm how the damage indicator grew larger in the TD than in the RD exhibiting the asymmetry that was described by the anisotropic fracture initiation criterion. In spite of this, the displacement corresponding to the fracture initiation point was prematurely predicted, 0.26 mm less than the onset of fracture displacement, by the criterion (see Fig. 17a).

4.5. Loading rate effects

Since a limited number of tests were conducted, the effect of the loading rate is analysed separately and only for the range of strain rates attained in such experiments and their corresponding finite element simulations. The equivalent plastic strains corresponding to the onset of fracture (or critical points) were plotted against the equivalent plastic strain rate in Fig. 18a for the NT5 and CH specimens and in Fig. 18b for the SH specimens for the three loading rates at which those were tested. A clear trend, where the fracture strain increased and subsequently decreased towards values that were close to the slow case fracture strains again with increasing strain rate could be observed in the NT5 and CH specimens. Conversely, the SH specimens did not exhibit any significant changes with increasing strain rate. Some other studies in similar alloys [49] suggest that if strain rates close to the largest experienced by the specimens in the

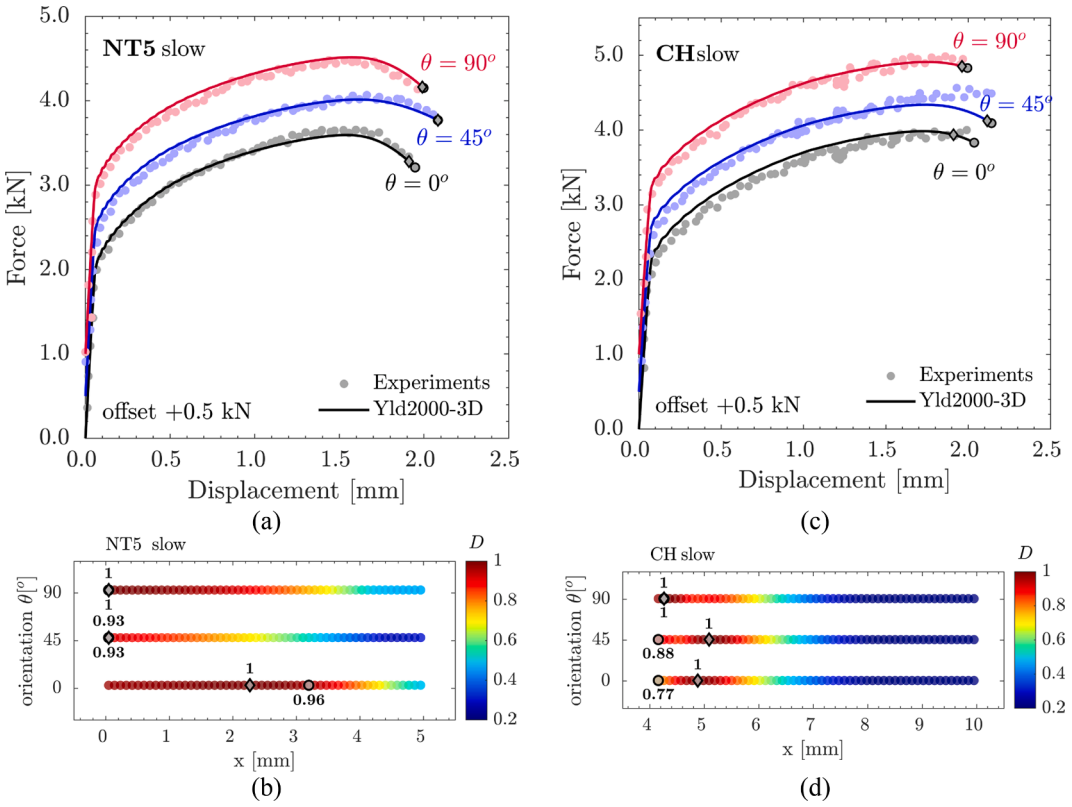

Fig. 15. (a and c) Force-displacement curves in which the critical and fracture initiation points are marked with a circle and a diamond respectively for the NT5 and CH specimens. (b and d) Damage indicator values of the elements located in the midplane centreline along the width of the specimens when first $D = 1$ or maximum value D was detected (indicated with a diamond in the force–displacement curves).

present investigation are achieved, dynamic strain aging effects might be milder or even disappear. This has been considered beyond of the scope of this investigation and further discussion on this topic can be found in recent publications [50–53].

The equivalent fracture strain for proportional loadings has been modified to accommodate the effects mentioned previously the constant b, that regulates the fracture strain for uniaxial tension and the constant c that modifies the shear fracture strain (see [20;29]) have been substituted for $b^*\left[\dot{\bar{\varepsilon}}_p\right]$ and $c^*\left[\dot{\bar{\varepsilon}}_p\right]$ respectively, two functions of the equivalent plastic strain rate as,

$$b^*\left[\dot{\bar{\varepsilon}}_p\right] = b\left(1 + \frac{d_1 \ln\left[\dot{\bar{\varepsilon}}_p/\dot{\varepsilon}_0\right]}{1 + \exp\left[d_2\left(\dot{\bar{\varepsilon}}_p - d_3\right)\right]}\right) \text{ and} \tag{27}$$

$$c^*\left[\dot{\bar{\varepsilon}}_p\right] = c\left(1 - \frac{d_1 \ln\left[\dot{\bar{\varepsilon}}_p/\dot{\varepsilon}_0\right]}{1 + \exp\left[d_2\left(\dot{\bar{\varepsilon}}_p - d_3\right)\right]}\right) \tag{28}$$

leading to the following modified expression,

$$\bar{\varepsilon}_f^{pr}\left[\tilde{\boldsymbol{\sigma}}/\bar{\sigma}, \dot{\bar{\varepsilon}}_p\right] = b^*\left[\dot{\bar{\varepsilon}}_p\right]\left(\frac{1 + c^*\left[\dot{\bar{\varepsilon}}_p\right]}{g[\tilde{\boldsymbol{\sigma}}/\bar{\sigma}]}\right)^{\frac{1}{n}} \tag{29}$$

The constants were calibrated with the same procedure as that employed in the quasi-static tests giving d_1=$d_2 = 1$ and$d_3 = 0.08$. The model predictions are plotted in the same fashion as those for the quasi-static tests in Fig. 19a and b. The predictions were reasonable for the specimens that showed good agreement with the plasticity model, being the exception the specimens that were oriented at 45°. Apart from the latter, there were two other cases that exhibited discrepancies between the model and the specimen simulations: the RD and the TD NT5 fast. Fig. 10c shows that the displacement applied to the finite element models was not enough to

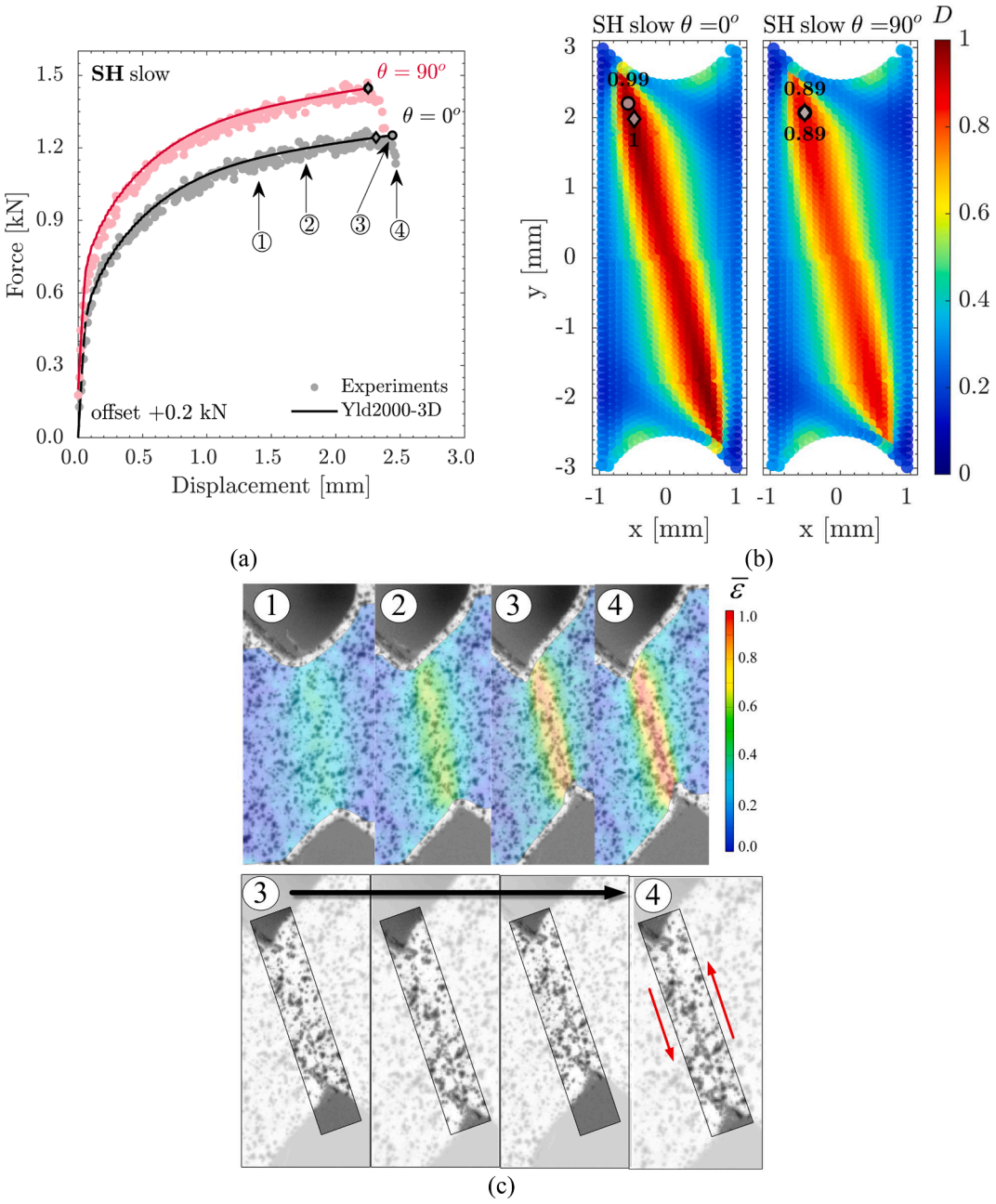

Fig. 16. (a) Force-displacement curves in which the critical and fracture initiation points are marked with a circle and a diamond respectively for the SH specimens. (b) Damage indicator values of the elements located on the surface of the specimens when first $D = 1$ or maximum value D was detected (indicated with a diamond in the force–displacement curves). (c-top) Equivalent von Mises plastic strain contours computed in the DIC software for the points indicated with circled numbers in the force–displacement curves. (c-bottom) Image sequence from ③ (visual crack initiation) to ④(fully developed crack).

overcome the notch effect in the NT5 specimens and deform it to the point where necking takes over and accumulates the plastic strain in the centre. It seemed that this particular fracture initiation criterion could not capture this effect. The fracture loci for proportional loadings and several constant strain rates are plotted in Fig. 20a and b to illustrate its effects in the predicted fracture strains.

5. Conclusions

An extensive experimental campaign has been performed that investigated the anisotropic mechanical behaviour of the AA5754 H111. Moreover, the effect that loading rates generating strain rates close to those observed in slow and production speed stamping

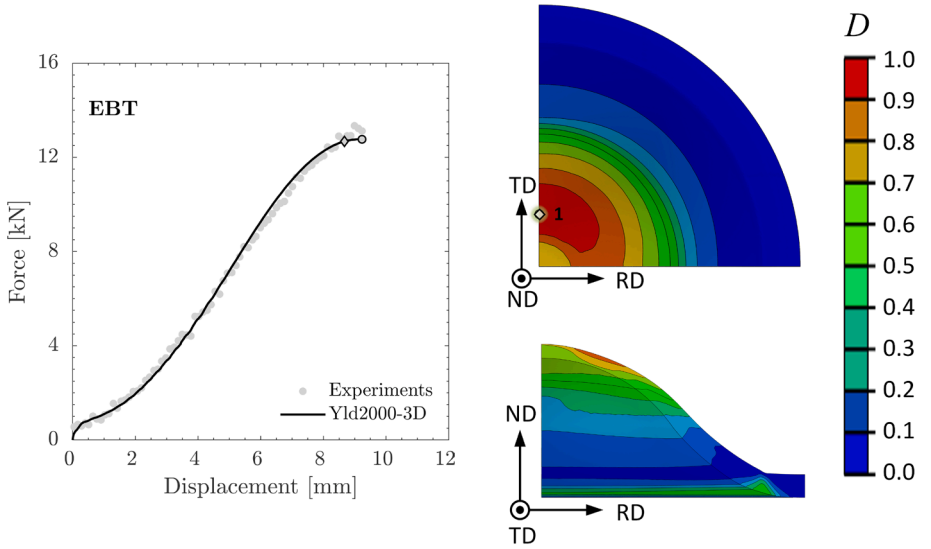

Fig. 17. (a) Force-displacement curve in which the critical and fracture initiation points are marked with a circle and a diamond respectively for the EBT specimens. (b) Damage indicator contours of the finite element simulations when first $D = 1$ was detected (indicated with a diamond in the force–displacement curves).

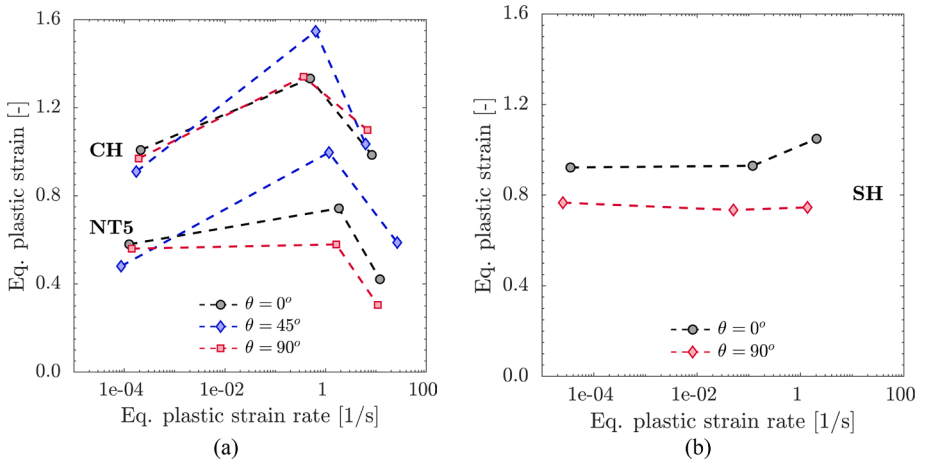

Fig. 18. Equivalent plastic strain to fracture extracted from the critical points in the finite element simulations from the slow, intermediate and fast cases of the NT5, CH (a) and SH (b) specimens.

processes have on the plasticity and fracture behaviours have been reported and discussed. Within this range of strain rates, it was found that the work hardening had a negative loading rate sensitivity, and that the fracture strains from the hybrid experimental–numerical approach exhibited a non-linear bell-shaped trend with increasing strain rates.

The anisotropic plasticity was modelled with the three-dimensional extension of the Yld2000 yield function with an associative flow rule and a negative rate-dependent work hardening that gave good agreement for a wide variety of specimens in three directions with respect to the RD and for varying loading rates compared to the experimental global (force–displacement curves) and local (logarithmic strains-displacement curves) responses. The anisotropic Hosford-Coulomb fracture initiation criterion was modified to include the strain rate effects and calibrated employing a hybrid experimental–numerical analysis. The criterion gave excellent predictions for the slow cases, while its performance for the intermediate and fast cases was acceptable but with room for improvement. This was mainly attributed to the specimen geometries and the choice of critical elements when calibrating the fracture models. Although valid for the range of strain rates studied, further testing at higher strain rates will help to establish more trends and extend the validity of the models.

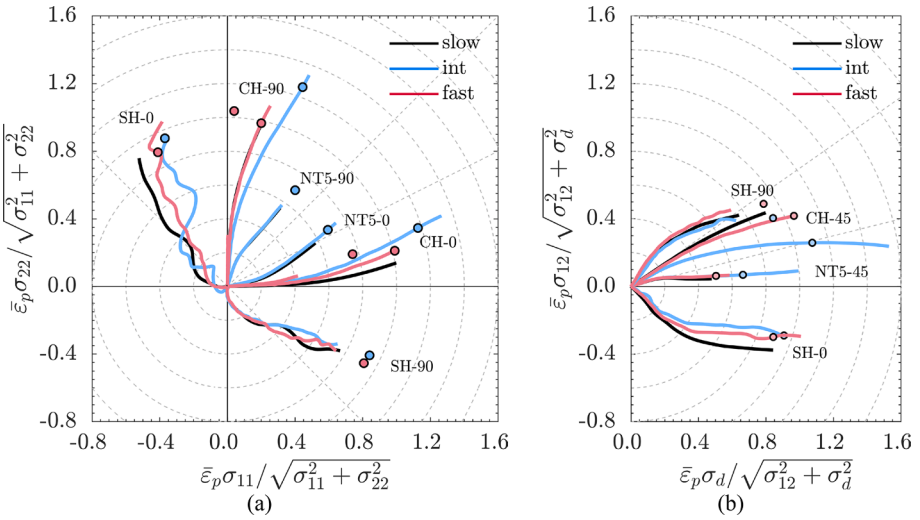

Fig. 19. Loading paths to fracture of the specimens under the so-called intermediate and fast loading conditions. The modified fracture initiation criterion's predictions are marked with circles.

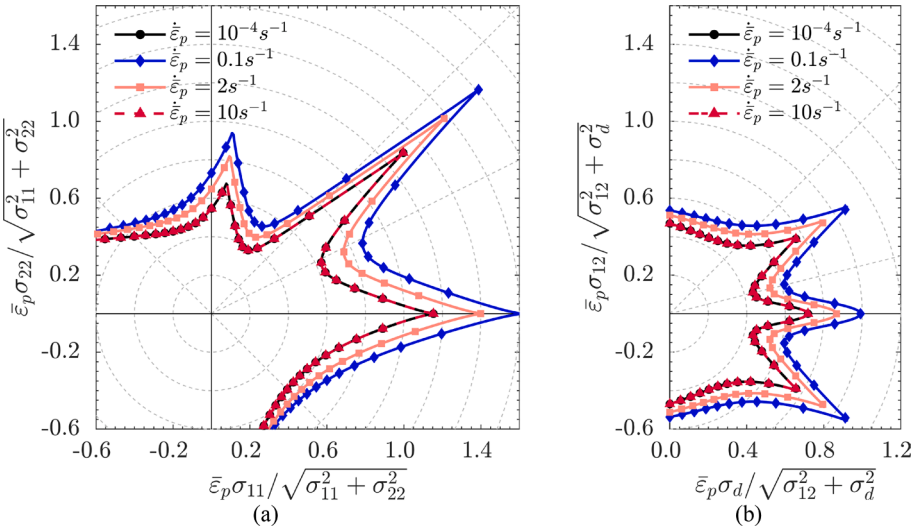

Fig. 20. Illustration of the loading rate effect in the anisotropic equivalent plastic strain to fracture for proportional loadings.

CRediT authorship contribution statement

Borja Erice: Conceptualization, Writing - Original Draft, Writing - Review & Editing, Investigation, Software, Supervision, Project administration. **Bernard Rolfe:** Project administration, Funding acquisition, Writing - Review & Editing. **Joseba Mendiguren:** Formal analysis, Investigation, Data Curation, Methodology, Writing - Review & Editing.

Declaration of Competing Interest

The authors declare the following financial interests/personal relationships which may be considered as potential competing interests: Borja Erice reports financial support was provided by Spain Ministry of Science and Innovation.

Data availability

Data will be made available on request.

Acknowledgements

The authors would like to thank Maddi Bueno for the preliminary testing. The author Borja Erice would like to acknowledge the support from the Grant RYC2021-033241-I funded by MCIN/AEI/ 10.13039/501100011033 and by "European Union NextGenerationEU/PRTR".

References

[1] Karafillis AP, Boyce MC. A general anisotropic yield criterion using bounds and a transformation weighting tensor. J Mech Phys Solids 1993;41:1859–86. https://doi.org/10.1016/0022-5096(93)90073-o.
[2] Barlat F, Aretz H, Yoon JW, Karabin ME, Brem JC, Dick RE. Linear transfomation-based anisotropic yield functions. Int J Plast 2005;21:1009–39. https://doi.org/10.1016/j.ijplas.2004.06.004.
[3] Aretz H, Barlat F. New convex yield functions for orthotropic metal plasticity. Int J Non Linear Mech 2013;51:97–111. https://doi.org/10.1016/J.IJNONLINMEC.2012.12.007.
[4] Cazacu O, Barlat F. Application of the theory of representation to describe yielding of anisotropic aluminum alloys. Int J Engng Sci 2003;41:1367–85. https://doi.org/10.1016/S0020-7225(03)00037-5.
[5] Cazacu O, Barlat F. Generalization of Drucker's Yield Criterion to Orthotropy. Http://DxDoiOrg/101177/108128650100600603 2001;6:613–30. https://doi.org/10.1177/108128650100600603.
[6] Yoshida F, Hamasaki H, Uemori T. A user-friendly 3D yield function to describe anisotropy of steel sheets. Int J Plast 2013;45:119–39. https://doi.org/10.1016/J.IJPLAS.2013.01.010.
[7] Soare S, Yoon JW, Cazacu O. On the use of homogeneous polynomials to develop anisotropic yield functions with applications to sheet forming. Int J Plast 2008;24:915–44. https://doi.org/10.1016/J.IJPLAS.2007.07.016.
[8] Hu W. An orthotropic yield criterion in a 3-D general stress state. Int J Plast 2005;21:1771–96. https://doi.org/10.1016/J.IJPLAS.2004.11.004.
[9] Dunand M, Maertens AP, Luo M, Mohr D. Experiments and modeling of anisotropic aluminum extrusions under multi-axial loading – Part I: Plasticity. Int J Plast 2012;36:34–49. https://doi.org/10.1016/J.IJPLAS.2012.03.003.
[10] D. Banabic Multiscale Modelling in Sheet Metal Forming 2016 Springer International Publishing Cham 10.1007/978-3-319-44070-5.
[11] Chu CC, Needleman A. Void nucleation effects in biaxially stretched sheets. J Eng Mater Technol-Trans ASME 1980;102:249–56.
[12] Tvergaard V, Needleman A. Analysis of the cup-cone fracture in a round tensile bar. Acta Metall 1984;32(1):157–69.
[13] Gurson AL. Continuum Theory of Ductile Rupture by Void Nucleation and Growth - Part I: Yield Criteria and Flow Rule. J Engng Mater Technol 1977;99:2–15.
[14] Lemaitre J. A continuous damage mechanics model for ductile fracture. J Eng Mater Technol-Trans ASME 1985;107:83–9.
[15] Brünig M, Chyra O, Albrecht D, Driemeier L, Alves M. A ductile damage criterion at various stress triaxialities. Int J Plast 2008;24:1731–55. https://doi.org/10.1016/J.IJPLAS.2007.12.001.
[16] Erice B, Gálvez F. A coupled elastoplastic-damage constitutive model with Lode angle dependent failure criterion. Int J Solids Struct 2014;51:93–110. https://doi.org/10.1016/j.ijsolstr.2013.09.015.
[17] Borvik T, Hopperstad OS, Berstad T, Langseth M. A computational model of viscoplasticity and ductile damage for impact and penetration. Eur J Mech A Solids 2001;20:685–712. https://doi.org/10.1016/S0997-7538(01)01157-3.
[18] Benzerga AA, Surovik D, Keralavarma SM. On the path-dependence of the fracture locus in ductile materials – Analysis. Int J Plast 2012;37:157–70. https://doi.org/10.1016/J.IJPLAS.2012.05.003.
[19] Lou Y, Huh H, Lim S, Pack K. New ductile fracture criterion for prediction of fracture forming limit diagrams of sheet metals. Int J Solids Struct 2012;49:3605–15. https://doi.org/10.1016/J.IJSOLSTR.2012.02.016.
[20] Mohr D, Marcadet SJ. Micromechanically-motivated phenomenological Hosford-Coulomb model for predicting ductile fracture initiation at low stress triaxialities. Int J Solids Struct 2015;67–68:40–55. https://doi.org/10.1016/j.ijsolstr.2015.02.024.
[21] Chocron S, Erice B, Anderson CECE, Chocron Erice B, Anderson CES, Chocron S, et al. A new plasticity and failure model for ballistic application. Int J Impact Eng 2011;38:755–64. https://doi.org/10.1016/j.ijimpeng.2011.03.006.
[22] Bai Y, Wierzbicki T. Application of extended Mohr-Coulomb criterion to ductile fracture. Int J Fract 2010;161:1–20. https://doi.org/10.1007/s10704-009-9422-8.
[23] Bao Y, Wierzbicki T. On fracture locus in the equivalent strain and stress triaxiality space. Int J Mech Sci 2004;46(1):81–98.
[24] Bai Y, Wierzbicki T. A new model of plasticity and fracture with pressure and Lode dependence. Int J Plast 2008;24:1071–96.
[25] Cockcroft MG, Latham DL. Ductility and Workability of Metals. J Inst Met 1968:33–9.
[26] Gruben G, Hopperstad OS, Børvik T. Evaluation of uncoupled ductile fracture criteria for the dual-phase steel Docol 600DL. Int J Mech Sci 2012;62:133–46. https://doi.org/10.1016/j.ijmecsci.2012.06.009.
[27] Luo M, Dunand M, Mohr D, Maertens AP, Luo M, Mohr D, et al. Experiments and modeling of anisotropic aluminum extrusions under multi-axial loading – Part I: Plasticity. Int J Plast 2012;36:36–58. https://doi.org/10.1016/j.ijplas.2012.03.003.
[28] Jia Y, Bai Y. Ductile fracture prediction for metal sheets using all-strain-based anisotropic eMMC model. Int J Mech Sci 2016;115–116:516–31. https://doi.org/10.1016/J.IJMECSCI.2016.07.022.
[29] Gu G, Mohr D. Anisotropic Hosford-Coulomb fracture initiation model: Theory and application. Engng Fract Mech 2015;147:480–97. https://doi.org/10.1016/j.engfracmech.2015.08.004.
[30] Li S, He Ji, Gu B, Zeng D, Xia ZC, Zhao Y, et al. Anisotropic fracture of advanced high strength steel sheets: Experiment and theory. Int J Plast 2018;103:95–118.
[31] Lou Y, Yoon JW. Anisotropic yield function based on stress invariants for BCC and FCC metals and its extension to ductile fracture criterion. Int J Plast 2018;101:125–55. https://doi.org/10.1016/J.IJPLAS.2017.10.012.
[32] Halim H, Wilkinson DS, Niewczas M. The Portevin–Le Chatelier (PLC) effect and shear band formation in an AA5754 alloy. Acta Mater 2007;55:4151–60. https://doi.org/10.1016/J.ACTAMAT.2007.03.007.
[33] Feng X, Fischer G, Zielke R, Svendsen B, Tillmann W. Investigation of PLC band nucleation in AA5754. Mater Sci Engng A 2012;539:205–10. https://doi.org/10.1016/J.MSEA.2012.01.082.
[34] Benallal A, Berstad T, Børvik T, Clausen AH, Hopperstad OS. Dynamic strain aging and related instabilities: experimental, theoretical and numerical aspects. Eur J Mech A Solids 2006;25:397–424. https://doi.org/10.1016/J.EUROMECHSOL.2005.10.007.
[35] Mazière M, Besson J, Forest S, Tanguy B, Chalons H, Vogel F. Numerical aspects in the finite element simulation of the Portevin–Le Chatelier effect. Comput Methods Appl Mech Engng 2010;199:734–54. https://doi.org/10.1016/J.CMA.2009.11.004.
[36] Bueno M, Galdos L, de Argandoña ES, Weiss M, Rolfe B, Lou Y, et al. Strain Rate Effect on the Fracture Behavior of the AA5754 Aluminum Alloy. Procedia Manuf 2020;47:1264–9.
[37] ISO 20482. ISO 20482:2013 - Metallic materials — Sheet and strip — Erichsen cupping test 2013. https://www.iso.org/standard/63857.html (accessed September 26, 2022).
[38] Barlat F, Brem JC, Yoon JW, Chung K, Dick RE, Lege DJ, et al. Plane stress yield function for aluminum alloy sheets—part 1: theory. Int J Plast 2003;19(9):1297–319.
[39] Wang WM, Sluys LJ, de Borst R. Viscoplasticity for instabilities due to strain softening and strain-rate softening. Int J Numer Meth Engng 1997;40:3839–64. https://doi.org/10.1002/(sici)1097-0207(19971030)40:20<3839::aid-nme245>3.0.co;2-6.
[40] ABAQUS/Explicit User's Manual, Version 6.14. United States: Dassault Systèmes Simulia Corp; 2014.

[41] Butcher C, Abedini A. Shear confusion: Identification of the appropriate equivalent strain in simple shear using the logarithmic strain measure. Int J Mech Sci 2017;134:273–83. https://doi.org/10.1016/J.IJMECSCI.2017.10.005.
[42] Erice B, Roth CC, Mohr D. Stress-state and strain-rate dependent ductile fracture of dual and complex phase steel. Mech Mater 2018;116:11–32. https://doi.org/10.1016/j.mechmat.2017.07.020.
[43] Ha J, Baral M, Korkolis YP. Ductile fracture of an aluminum sheet under proportional loading. J Mech Phys Solids 2019;132:103685. https://doi.org/10.1016/j.jmps.2019.103685.
[44] Lou Y, Huh H. Extension of a shear-controlled ductile fracture model considering the stress triaxiality and the Lode parameter. Int J Solids Struct 2013;50:447–55. https://doi.org/10.1016/j.ijsolstr.2012.10.007.
[45] Qian LY, Fang G, Zeng P. Modeling of the ductile fracture during the sheet forming of aluminum alloy considering non-associated constitutive characteristic. Int J Mech Sci 2017;126:55–66. https://doi.org/10.1016/J.IJMECSCI.2017.03.013.
[46] Fourmeau M, Børvik T, Benallal A, Hopperstad OS. Anisotropic failure modes of high-strength aluminium alloy under various stress states. Int J Plast 2013;48:34–53. https://doi.org/10.1016/J.IJPLAS.2013.02.004.
[47] Defaisse C, Mazière M, Marcin L, Besson J. Ductile fracture of an ultra-high strength steel under low to moderate stress triaxiality. Engng Fract Mech 2018;194:301–18. https://doi.org/10.1016/J.ENGFRACMECH.2017.12.035.
[48] Dunand M, Mohr D. Hybrid experimental–numerical analysis of basic ductile fracture experiments for sheet metals. Int J Solids Struct 2010;47:1130–43. https://doi.org/10.1016/j.ijsolstr.2009.12.011.
[49] Abbadi M, Hähner P, Zeghloul A. On the characteristics of Portevin–Le Chatelier bands in aluminum alloy 5182 under stress-controlled and strain-controlled tensile testing. Mater Sci Engng A 2002;337:194–201. https://doi.org/10.1016/S0921-5093(02)00036-9.
[50] S.M. Keralavarma A.F. Bower W.A. Curtin Quantum-to-continuum prediction of ductility loss in aluminium–magnesium alloys due to dynamic strain aging Nat Commun 5 1.
[51] Pandey A, Khan AS, Kim EY, Choi SH, Gnäupel-Herold T. Experimental and numerical investigations of yield surface, texture, and deformation mechanisms in AA5754 over low to high temperatures and strain rates. Int J Plast 2013;41:165–88. https://doi.org/10.1016/J.IJPLAS.2012.09.006.
[52] Xu J, Holmedal B, Hopperstad OS, Mánik T, Marthinsen K. Dynamic strain ageing in an AlMg alloy at different strain rates and temperatures: Experiments and constitutive modelling. Int J Plast 2022;151:103215. https://doi.org/10.1016/J.IJPLAS.2022.103215.
[53] Ren SC, Morgeneyer TF, Mazière M, Forest S, Rousselier G. Effect of Lüders and Portevin–Le Chatelier localization bands on plasticity and fracture of notched steel specimens studied by DIC and FE simulations. Int J Plast 2021;136:102880. https://doi.org/10.1016/J.IJPLAS.2020.102880.